ROBUST FAULT DETECTION AND ISOLATION USING A PARITY EQUATION IMPLEMENTATION OF DIRECTIONAL RESIDUALS

by

Maira Omana

Bachelor in Electrical Engineering
Universidad Industrial de Santander, 2001

A Thesis Submitted in Partial Fulfilment of
the Requirements for the Degree of

Master of Science

in the Graduate Academic Unit of Electrical Engineering

Supervisor: James H. Taylor, PhD, Electrical and Computer Engineering

Examining Board: Bruce G. Colpitts, PhD, Electrical and Computer Engineering
Eugene F. Hill, PhD, Electrical and Computer Engineering
Rickey Dubay, PhD, Mechanical Engineering

This thesis is accepted by the
Dean of Graduate Studies

THE UNIVERSITY OF NEW BRUNSWICK

December, 2005

© Maira Omana, 2006

To my parents, my aunt, my brother and my sister,
who offered me unconditional love and support
throughout the course of this thesis

ABSTRACT

Fault detection and isolation (FDI) has been an important field of research in the control engineering community for the last two decades. Its significance is based on enhancements in terms of safety, reliability and operating costs of the plant.

This research focuses on solving the failure detection and isolation (FDI) problem by developing a model-based approach using a parity equation implementation of directional residuals. This new approach is an extension of the generalized parity vector (GPV) technique based on the stable factorization. The present research has improved the approach in Viswanadham, Taylor and Luce [21] in three important aspects. First, a novel transformation matrix computation is presented that enhances the isolation properties of the FDI algorithm, i.e., increases the maximum number of faults that can be isolated and the number of disturbances that can be decoupled above the number of outputs of the system [7]. Second, disturbance decoupling is implemented in the stable factorization framework to make the residuals immune to measurable disturbance effects. Third, an adaptive threshold logic was developed and implemented to take into account modeling errors.

The efficacy and robustness of this technique is demonstrated by applying this FDI scheme to a jacketed continuously stirred tank reactor (JCSTR).

ACKNOWLEDGMENTS

I would like to especially thank Dr. James H. Taylor without whom this thesis would not exist. From the formative stages of this thesis, to the final draft, I owe him an immense amount of gratitude. His sage advice, insightful criticisms, and patient encouragement aided the writing of this thesis in innumerable ways.

This project is supported by Atlantic Canada Opportunities Agency (ACOA) under the Atlantic Innovation Fund (AIF) program. I gratefully acknowledge that support and the collaboration of the Cape Breton University (CBU), the National Research Council (NRC) of Canada, and the College of the North Atlantic (CNA).

Sincere appreciation is extended to Mr. Atalla Sayda for his valuable contributions and encouragement for the successful culmination of this research.

I would like to express my sincere appreciation to the faculty and staff of the Department of Electrical and Computer Engineering at University of New Brunswick for their patience and continuous encouragement. For her effort and assistance, a special thanks to Ms. Denise Burke for her kindness and support during my master program.

I would also like to thank my best friend, Pilar Moreno, for her friendship and unconditional support during the most challenging situations.

Special thanks to my family, who loved and supported me all the way since the beginning of my studies.

To each of the above, I extend my deepest appreciation

Fredericton, New Brunswick *Maira Omana*
December, 2005

TABLE OF CONTENTS

List of Tables

List of Figures

List of Symbols and Abbreviations

Symbols

$a_i(t)$	i^{th} actuator error
A, B, C, E	State space matrices
b_j	Constant bias in the j^{th} actuator
B^j	j^{th} column of matrix B
B_n^{hv}	Heating fluid inflow valve reference direction
B_n^j	j^{th} actuator reference direction
B_n^{ov}	Outflow valve reference direction
$\tilde{B}$	Extended B matrix
$c_{eq}(T_r)$	Nonlinear equality constraints
c_i	Constant bias in the i^{th} sensor
$c(T_r)$	Nonlinear inequality constraints
$d(t)$	Disturbance vector
f_a^j	j^{th} actuator fault
f_s^i	i^{th} sensor fault
$F_{i,j}$	Objective function for T_r calculation
F_{in}	Mixture inflow
F_{Jin}	Jacket heating fluid inflow
G	Disturbance matrix
$\lvert GPV \rvert$	Generalized parity vector magnitude

$\|GPV\|_{ff}$	Fault free GPV magnitude
$\angle GPV_k$	Angle between the GPV and the k^{th} reference direction
K, F	Stabilizing gain matrices
N_p, D_p	Alternative notation for the right coprime factors
$N(s)$, $D(s)$	Right coprime factors
N_{sp}^i	Normal to the i^{th} Sensor reference plane
$\tilde{N}_p$, $\tilde{D}_p$	Alternative notation for the left coprime factors
$\tilde{N}(s)$, $\tilde{D}(s)$	Left coprime factors
$p_{a,j}(s)$	Parity relation for a fault in the j^{th} actuator
$p_{a,j}^{ss}(s)$	Steady state parity relation for a fault in the j^{th} actuator
$p_{s,i}(s)$	Parity relation for a fault in the i^{th} sensor
$p_{s,i}^{ss}(s)$	Steady state parity relation for a fault in the i^{th} sensor
$p(s)$	Generalized parity vector
$P(s)$	Transfer function matrix
r^2	Coefficient of determination
$s_i(t)$	i^{th} sensor error
SP^i	i^{th} sensor reference plane
SP^t	Temperature sensor reference plane
SP^v	Volume sensor reference plane
T_h	Threshold
T_{in}	Mixture inlet temperature
T_{Jin}	Heating fluid inlet temperature
T_r	Transformation matrix
$\|T_r\|$	Transformation matrix magnitude
$u_d(s)$	Desired control input
$u(t)$	Input vector
$\tilde{u}(t)$	Extended input vector

$x(t)$	State vector
$y_d(s)$	Actual plant output
$y(s)$	Sensor output
Z_i	i^{th} transformed reference direction
Δ_a	Differential actuator angle threshold
Δ_s	Differential sensor angle threshold
ΔT	Temperature setpoint variation
ΔV	Volume setpoint variation
Θ_i	Angle between the GPV and the i^{th} sensor reference plane
Θ_j	Angle between the GPV and the j^{th} actuator reference direction
σ	Stabilizing pole shift

Abbreviations

Cond	Condition number
FDI	Fault detection and isolation
GPV	Generalized parity vector
JCSTR	Jacketed continuously stirred tank reactor

Chapter 1

Introduction

The continuous and growing advances in process control have resulted in large and complex plants, increasing the need of high performance fault monitoring systems. As a result, fault detection and isolation has become a critical issue for safe and reliable plant operation and reduction of economic losses. Several techniques using quantitative model-based methods [18], qualitative model-based methods [17] and history-based methods [19] have been developed. They have attempted to achieve faster detection times with lower false alarm and misdetection rates during the fault isolation process, in the presence of noise and disturbances [9]. The suitability of each technique depends on the plant characteristics and model availability. The general description of a fault detection and isolation system is illustrated in Fig. 1.1

This thesis focuses on the development of a model-based approach using a parity equation implementation of directional residuals for solving the FDI problem. The stages of model-based FDI using the GPV technique are illustrated in Fig. 1.2. The research on the fault detection and isolation problem using model-based approaches dates back to the 1970's, when the aerospace fault detection community introduced

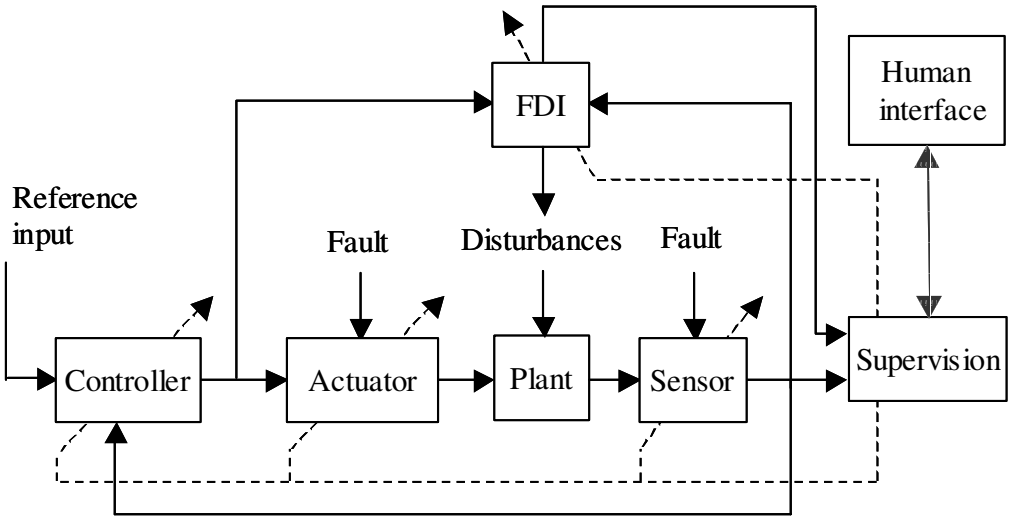

Figure 1.1: Description of an FDI system

the concept of analytical redundancy. The basic idea of the analytical redundancy approach is to compare the actual behavior of the plant with that predicted by the mathematical plant model [2], [5], [4], [22]. The resulting inconsistency is called the residual, which should be close to zero when no fault occurs. However, it shows a significant change when abnormal plant behavior is detected [6].

In 1976, dynamic parity relations were introduced by Willsky [22], yielding a systematic development of analytical redundancy provided by the mathematical model of the plant. Later on, Chow and Willsky [2] proposed a procedure to generate parity equations from the state-space representation of a dynamic system. Gertler and Singer [8] extended it to statistical isolability under noisy conditions and generalized the isolability criteria by simultaneously minimizing the sensitivity of residuals to small drifts in cases having only additive plant faults.

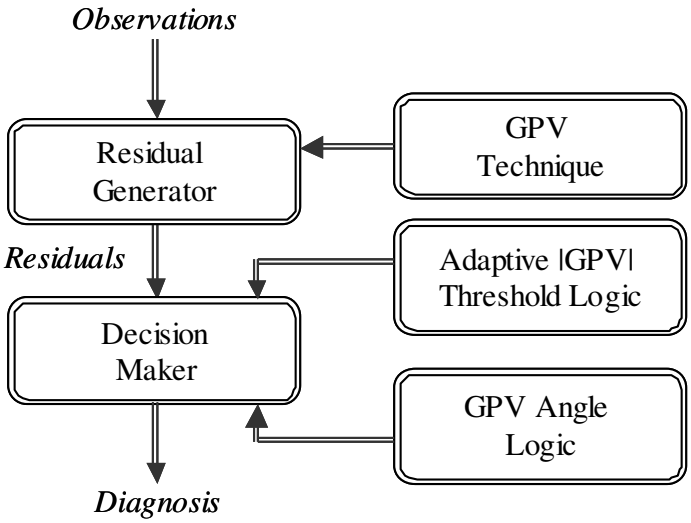

Figure 1.2: Stages of model-based FDI

While previous approaches were able to detect the faults of a system, there was a need to generate enhanced residuals, which were not only fault sensitive but also fault selective. For the purpose of isolation, Viswanadham, Taylor and Luce [21] introduced the generation of directional residuals using the GPV technique for FDI. The idea of this approach is that each failure will result in activity of the parity vector along certain directions or in certain subspaces [7], [10], [14] and [21]. Therefore, the fault isolation amounts to determining which predefined direction the parity vector is most nearly aligned with.

As another strategy for solving the isolation issue, a structural residual approach was proposed by Gertler and Singer [8]. It was designed in such a way that each residual responds to a subset of faults selectively allowing the formation of binary fault signatures.

Several authors have done further research during the past years regarding the stability and realizability of the residual generator, as well as its robustness. This has allowed the model-based approaches to be reliable for FDI despite the difficulty and errors involved in the modeling of complex plants. The present work solves the FDI problem using an extension of the generalized parity vector (GPV) technique based on the stable factorization approach which ensures a stable residual generator [21].

In chapter 2 a general overview of stable factorization is first given, followed by its application to implement the generalized parity vector technique. In chapter 3, FDI using directional residuals for sensor and actuator faults is presented, together with the implementation of disturbance decoupling in the stable factorization framework. In chapter 4 a novel calculation of the transformation matrix is proposed to enhance the FDI properties. In chapter 5, four different techniques are presented to implement the decision maker block. Finally, chapters 6 and 7, present the results for FDI robustness and overall performance, respectively, based on application to a jacketed continuously stirred tank reactor (JCSTR).

Chapter 2

Residual Generation Using the Generalized Parity Vector Technique

2.1 Introduction

Quantitative model-based failure detection and isolation (FDI) methods rely on the comparison of a system's available measurements, with *a priori* information represented by the system's mathematical model. There are two main trends of this approach: analytical redundancy or residual generation methods and parameter estimation [14]. In the present work, the FDI methodology is developed based on residual generation.

Since quantitative model-based methods for FDI are developed based on some fundamental understanding of the physics of the process, FDI using analytical redundancy methods is a viable implementation for systems where *a priori* knowledge is available in terms of mathematical functional relationships between the inputs and outputs of the system [18].

While there are several methods for residual generation, this work is focused on residual generation using the generalized parity vector (GPV) technique, which is developed in the stable factorization framework. Before introducing the GPV concept, some of the fundamental mathematics of stable factorization are outlined.

2.2 Stable factorization

The significance of using the stable coprime factorization approach is that the parity relations obtained involve stable, proper and rational transfer functions even for unstable plants. Therefore the realizability and stability of the residual generator is guaranteed. Given any $n \times m$ proper rational transfer function matrix *P(s)*, it can be defined in terms of its right and left coprime factors as follows [1]:

$$P(s) = N(s)D(s)^{-1} \tag{2.1}$$

$$P(s) = \tilde{D}(s)^{-1}\tilde{N}(s) \tag{2.2}$$

where *N(s)* and *D(s)* are said to be right coprime factors, and $\tilde{N}(s)$ and $\tilde{D}(s)$ are called the left coprime factors. All factors belong to the set of stable transfer function matrices. For both cases, this implies that the matrix extension of the Bezout identity holds:

$$X(s)N(s) + Y(s)D(s) = I \tag{2.3}$$

$$\tilde{X}(s)\tilde{N}(s) + \tilde{Y}(s)\tilde{D}(s) = I \tag{2.4}$$

where *X(s)*, *Y(s)*, $\tilde{X}(s)$ and $\tilde{Y}(s)$ are also in the set of stable transfer function matrices. Equating the left and right descriptions of *P(s)* given in equations (2.1) and (2.2), the following identity holds:

$$\tilde{D}N - \tilde{N}D = 0 \tag{2.5}$$

Combining the identities in equations (2.3), (2.4) and (2.5), the double coprime factorization of *P(s)* is defined as follows:

$$\begin{bmatrix} Y(s) & X(s) \\ -\tilde{N}(s) & \tilde{D}(s) \end{bmatrix} \begin{bmatrix} D(s) & -\tilde{X}(s) \\ N(s) & \tilde{Y}(s) \end{bmatrix} = \begin{bmatrix} I & 0 \\ 0 & I \end{bmatrix} \tag{2.6}$$

The two block matrices in the left-hand side of (2.6) are unimodular, and each one is the inverse of the other. A unimodular matrix is a real square matrix with determinant equal to one. More generally, a matrix with elements in the polynomial domain $F(s)$ is called unimodular if it has an inverse whose elements are also in $F(s)$. A matrix is therefore unimodular iff its determinant is a unit of $F(s)$. As a result, the matrix inverse of a unimodular real matrix is another unimodular matrix [12]. Equation (2.6) is called the generalized Bezout identity [21].

2.2.1 Stable factors from state-space representations

The GPV technique is based on the stable factorization of the system transfer function matrix in terms of its state-space representation. Let the system be described by the set of equations:

$$\dot{x}(t) = Ax(t) + Bu(t) + Gd(t) \tag{2.7}$$
$$y(t) = Cx(t) + Eu(t) \tag{2.8}$$

where x, u, d, and y represent the state variables, inputs, disturbances and outputs of the system, respectively and *A, B, G, C, E* are matrices of compatible dimensions.

The transfer matrix of this system (assuming no disturbances acting on the plant) is:

$$P(s) = C(sI - A)^{-1}B + E \tag{2.9}$$

The objective is to derive a doubly coprime factorization of P, as it is given in Theorem (2.2.1) below [20]:

Theorem 2.2.1. *Given the system (2.7)-(2.8), suppose the pairs (A, B) and (A, C) are stabilizable and detectable, respectively. Select constant matrices K and F, such that the matrices* $A_o : A - BK$, $\tilde{A}_o : A - FC$ *are both Hurwitz. Then* $P = N_p D_p^{-1} = \tilde{D}_p^{-1}\tilde{N}_p$ *and*

$$\begin{bmatrix} Y & X \\ -\tilde{N}_p & \tilde{D}_p \end{bmatrix} \begin{bmatrix} D_p & -\tilde{X} \\ N_p & \tilde{Y} \end{bmatrix} = \begin{bmatrix} I & 0 \\ 0 & I \end{bmatrix} \tag{2.10}$$

where the various matrices are defined as follows:

$$\begin{aligned}
\tilde{N}_p &= C(sI - \tilde{A}_o)^{-1}(B - FE) + E && (2.11)\\
\tilde{D}_p &= I - C(sI - \tilde{A}_o)^{-1}F && (2.12)\\
N_p &= (C - EK)(sI - A_o)^{-1}B + E && (2.13)\\
D_p &= I - K(sI - A_o)^{-1}B && (2.14)\\
X &= K(sI - \tilde{A}_o)^{-1}F && (2.15)\\
Y &= I + K(sI - \tilde{A}_o)^{-1}(B - FE) && (2.16)\\
\tilde{X} &= K(sI - A_o)^{-1}F && (2.17)\\
\tilde{Y} &= I + (C - EK)(sI - A_o)^{-1}F && (2.18)
\end{aligned}$$

■

Using the definition given in equations (2.11) and (2.12), the left coprime factors $\tilde{N}_p$ and $\tilde{D}_p$ are renamed for simplicity hereafter as $\tilde{N}$ and $\tilde{D}$ and rewritten as follows:

$$\begin{aligned}
\tilde{N} &= C(sI - \tilde{A}_o)^{-1}(B - FE) + E && (2.19)\\
\tilde{D} &= I - C(sI - \tilde{A}_o)^{-1}F && (2.20)
\end{aligned}$$

2.3 Generalized parity vector technique

Consider the linear time invariant plant depicted in Fig. 2.1, which is described by the $p \times m$ transfer function matrix *P(s)*. Let u_d be the desired or correct control input and u be the actual plant input (output of the actuator). The relation between u and u_d is given by equation (2.21):

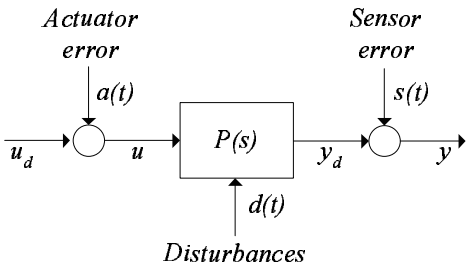

Figure 2.1: LTI system with disturbances, sensor and actuator failure models

$$u(t) = u_d(t) + a(t) \tag{2.21}$$

where *a(t)* is a time-varying vector with elements $a_i(t)$ representing various failure modes of the i^{th} actuator. Similarly, let y_d be the actual output of the plant (desired or correct sensor output) and y to be the actual output of the sensor. The relation between these variables is expressed in equation (2.22):

$$y(t) = y_d(t) + s(t) \tag{2.22}$$

where *s(t)* is a time-varying vector with elements $s_i(t)$ representing sensor failures. The variables u_d, y and d are "external" or available for FDI, while u and y_d are "internal" or unaccessible. The relationship among these signals is depicted in Fig. 2.1.

Based on the system in Fig. 2.1, the definition of the transfer function matrix *P(s)* given in equation (2.2) and taking the relationship among the desired control input, u_d, and the actual output of the sensors, y, the following relations are obtained:

$$P(s) = \tilde{D}(s)^{-1}\tilde{N}(s) = \frac{y(s)}{u_d(s)} \tag{2.23}$$

$$\tilde{D}(s)y(s) - \tilde{N}(s)u_d(s) = 0 \tag{2.24}$$

Under ideal conditions, when the plant is linear, noise and fault free, equation (2.24) holds. However, when a fault happens, this relation is violated showing the inconsistency between the actuator inputs and sensor outputs with respect to the unfailed model. Using this fact, the generalized parity vector, *p(s)*, is defined as:

$$p(s) = T_r(s)[\tilde{D}(s)y(s) - \tilde{N}(s)u_d(s)] \tag{2.25}$$

The GPV is a time varying function of small magnitude under normal operating conditions, due to the presence of noise and modeling errors arising from linearization and order reduction. However, it exhibits a significant magnitude change when a fault occurs. Each distinct failure produces a parity vector with different characteristics, allowing the use of the GPV for isolation purposes.

A transformation matrix $T_r(s)$ is introduced in equation (2.25) to improve fault isolability. The present work is focused on fault diagnosis using the direction of the parity vector under various failure conditions. We assume hereafter that T_r is constant, and that F in equations (2.19) and (2.20) is chosen such that $\tilde{A}_o = -\sigma I$ (which can always be done if *(A, C)* is observable); this simplifies our discussion of GPV behavior [21].

Chapter 3

Fault Detection and Isolation Using Directional Residuals

3.1 Introduction

The basic idea of FDI using failure directions is that each failure will result in activity of the parity vector along certain axes or in certain subspaces. These reference axes or subspaces are determined by the state space matrices. This information can be used to isolate the fault with fewer parity variables than required using voting based on parity variables magnitude alone; therefore, in many cases this approach is much simpler to implement than a voting scheme. Depending on the dynamics of the system, some of these reference directions may be close or identical, making the isolation for some faults difficult or unachievable. To overcome the angle separation problem between the reference directions, the calculation of an optimal transformation matrix T_r is introduced in chapter 4.

3.2 Actuator faults

In order to analyze actuator FDI, an additive fault $a_j(t)$ of the form described in equation (2.21) is assumed in the j^{th} actuator. Substituting equation (2.21) into (2.25) and noting that $\tilde{D}y - \tilde{N}u_d = 0$, the following relation is obtained:

$$p_{a,j}(s) = -(T_r\tilde{N})^j a_j(t) \tag{3.1}$$

Equation (3.1) shows that $p_{a,j}(s)$ is restricted to exhibit activity along the direction defined by the j^{th} column of $T_r\tilde{N}$. For a system with $y{=}x$, or state space matrices $C = I_{n\times n}$ and $E = 0_{n\times m}$, as in the JCSTR model, equation (2.19) can be rewritten more simply as:

$$\tilde{N} = (sI - \tilde{A}_o)^{-1}B = [diag(s+\sigma)]^{-1}B \tag{3.2}$$

Using equation (3.2), equation (3.1) can be rewritten as follows:

$$p_{a,j}(s) \triangleq T_r B^j \frac{a_j(s)}{s+\sigma} \tag{3.3}$$

Comparing equations (3.1) and (3.3), the j^{th} actuator reference direction, B_n^j, is defined as $B_n^j = B^j$. Therefore equation (3.3) can be written in terms of the the j^{th} actuator reference direction as:

$$p_{a,j}(s) \triangleq T_r B_n^j \frac{a_j(s)}{s+\sigma} \tag{3.4}$$

Assuming a step or bias failure in the j^{th} actuator, and since $\tilde{N}(s)$ and $\tilde{D}(s)$ are stable matrices, the steady-state parity vector, p^{ss}, can be computed using the final value theorem [21] according to equation (3.5).

$$\lim_{s\to 0} sp(s) = \lim_{t\to\infty} p(t) = p^{ss} \tag{3.5}$$

Thus, for a constant bias of magnitude b_j on the j^{th} actuator, the $p_{a,j}^{ss}$ is given by:

$$\lim_{s\to 0}\left\{ -T_r B_n^j \left[\frac{b_j/s}{s+\sigma}\right] s \right\} = \lim_{t\to\infty} p(t) \tag{3.6}$$

$$p_{a,j}^{ss} = -T_r B_n^j \frac{b_j}{\sigma} \tag{3.7}$$

The actuator fault isolation is based on the angle Θ_j between the GPV and B_n^j as illustrated in Fig. 3.1. If the j^{th} actuator is faulty, this angle should be zero in the ideal case or less than a small threshold value, T_h, to account for model uncertainty.

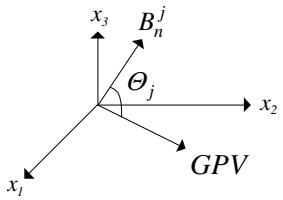

Figure 3.1: Actuator FDI

3.3 Sensor faults

Similarly, to explain sensor FDI an additive fault $s_i(t)$, of the form described in equation (2.22) is applied to the i^{th} sensor. Based on this assumption, the parity vector in equation (2.3) reduces to:

$$p_{s,i}(s) = (T_r \tilde{D})^i s_i(t) \tag{3.8}$$

Assuming the same state space representation used in section 3.2, $C = I$ and $(sI - \tilde{A}_o) = [diag(s+\sigma)]$, equation (2.20) can be simplified as:

$$\tilde{D} = I - (sI - \tilde{A}_o)^{-1} F = I - [diag(s+\sigma)^{-1}] F \tag{3.9}$$

Recalling that $\tilde{A}_o = A - FC = [diag\,(-\sigma)] = -\sigma I$ and substituting $C = I$ yields $F = A + \sigma I$, so equation (3.9) can be rewritten as follows:

$$\tilde{D} = I - [diag(s+\sigma)^{-1}][A + \sigma I] \tag{3.10}$$

To simplify equation (3.10) the vectors E_d and B_d are defined as:

$$B_d = (-A - \sigma I)\,,\; E_d = I \tag{3.11}$$

Using the previous definitions, equation (3.8) can be rewritten in terms of the vectors which define the sensor reference plane as:

$$p_{s,i}(s) = T_r \left[E_d^i + \frac{B_d^i}{s+\sigma} \right] s_i(s) \tag{3.12}$$

Thus, for the sensor failure case, it is not possible to confine $p_{s,i}(s)$ to lie along a fixed axis. Only for fortuitous cases, depending on the dynamics of the system, can this be achieved. However, for any system, the GPV always lies in a plane of the generalized parity space, defined by the column vectors E_d^i and B_d^i.

As in actuator FDI, assuming a step or bias failure in the i^{th} sensor, the steady-state parity vector, p^{ss}, can be computed using the final value theorem [21] according to equation (3.5). For a constant bias of magnitude c_i on the i^{th} sensor, the $p_{s,i}^{ss}$ is given by:

$$\lim_{s\to 0}\; sT_r \left[E_d^i + \frac{B_d^i}{s+\sigma} \right] \frac{c_i}{s} \;=\; \lim_{t\to\infty}\; p(t) = p_{s,i}^{ss} \tag{3.13}$$

$$p_{s,i}^{ss} = T_r B_s^{\,i}\, \frac{c_i}{\sigma} \tag{3.14}$$

where

$$B_s^i = \sigma E_d^i + B_d^i \tag{3.15}$$

The sensor fault isolation is based on the angle Θ_i, between the GPV and the i_{th} sensor reference plane, SP^i, as illustrated in Fig. 3.2. If the i^{th} sensor is faulty, this angle should be zero or less than T_h.

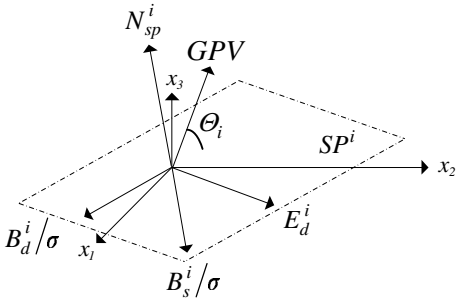

Figure 3.2: Sensor FDI

3.4 Special case for sensor-actuator faults

We consider a special case in terms of the actuator direction B_n^j and the SP^i normal, N_{sp}^i shown in Fig. 3.2 and defined by $N_{sp}^i = E_d^i \otimes B_d^i$ as:

$$B_n^j \cdot N_{sp}^i = 0 \tag{3.16}$$

If the dot product of B_n^j and the normal to the i^{th} sensor reference plane is zero then the j^{th} actuator axis lies on the i^{th} sensor reference plane [11] as is illustrated in Fig. 3.3. This condition would be a result of the system state space structure. For this case it is not possible to calculate a transformation matrix T_r such as the actuator reference direction can be taken out of the sensor reference plane. This can be demonstrated mathematically by proving equation (3.17) for arbitrary T_r, which was done by symbolic manipulation in MATLAB®. From this proof it is concluded

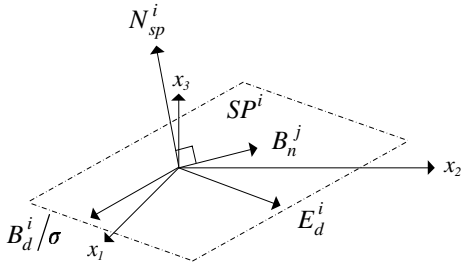

Figure 3.3: Special case for Sensor-Actuator FDI

that equation (3.17) holds for any transformation matrix T_r, which means that the j^{th} actuator reference direction will always lie on the i^{th} sensor reference plane.

$$T_r B^j_n \cdot (T_r E^i_d \otimes T_r B^i_d) = 0 \tag{3.17}$$

Under this circumstance we may still be able to distinguish between these faults by taking a more detailed look at the parity vector relation in equation (3.12): Let us assume that $s_i(s) = c_i/s$ (a bias fault) [21]; we can apply the initial value theorem to show that the initial GPV activity is in the direction $T_r E^i_d$, as follows:

$$\lim_{s\to\infty} sT_r \left[E^i_d + \frac{B^i_d}{s+\sigma} \right] \frac{c_i}{s} = \lim_{t\to 0} p(t) = p^o_{s,i} \tag{3.18}$$

$$p^o_{s,i} = T_r E^i_d \, c_i \tag{3.19}$$

and invoke the results obtained in equations (3.13), (3.14) and (3.15) using the final value theorem, to demonstrate that the steady-state GPV activity is in the direction $T_r \left[E^i_d + \frac{B^i_d}{\sigma} \right] \triangleq T_r B^i_s$. Thus $p^{ss}_{s,i}$ and $p^o_{s,i}$ define a sector in the plane SP^i that encompasses the dynamic behavior of $p_{s,i}$.

This was demonstrated for the JCSTR example by applying volume and temperature sensor faults at *t=0.5 hours*. Figures 3.4 and 3.5 show that after the fault is

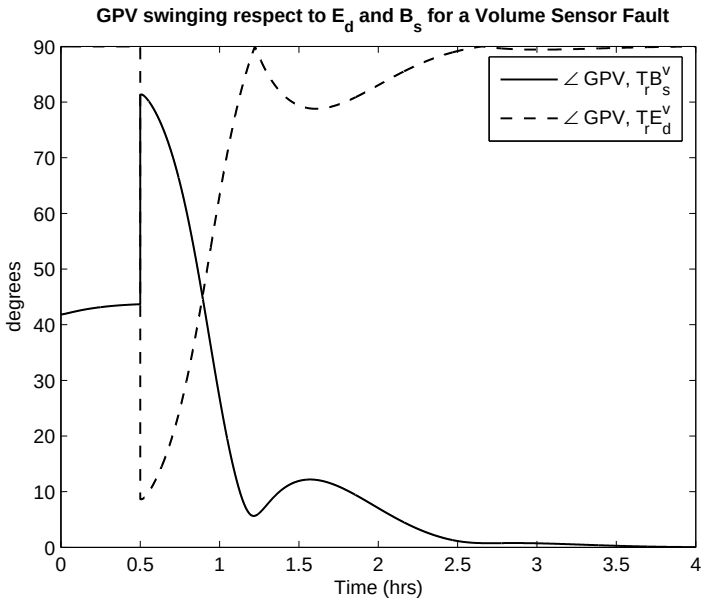

Figure 3.4: $\measuredangle\left(GPV, T_r E_d\right)$ and $\measuredangle\left(GPV, T_r B_s\right)$ for a Volume Sensor Fault

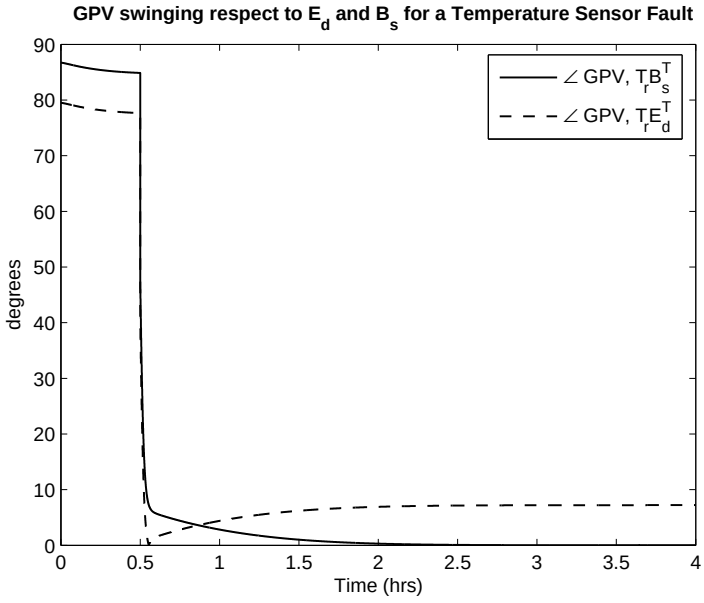

Figure 3.5: $\measuredangle\left(GPV, T_r E_d\right)$ and $\measuredangle\left(GPV, T_r B_s\right)$ for a Temperature Sensor Fault

applied, the angle between the GPV and B_s approaches zero, while the angle between the GPV and E_d moves apart. Thus the GPV swinging from E_d to B_s for the faulty case is shown. However, this is only valid for the pure linear case.

Nevertheless, we can still clearly isolate the i^{th} sensor fault from the j^{th} actuator fault unambiguously as long as B_n^j is not in or near the cone angle (sector) between E_d^i and B_s^i [13], using the following logic:

$$\left.\begin{array}{l} if\ \measuredangle(GPV, SP^i) \leq T_h\ then \\ \quad if\ \measuredangle(GPV, B_n^j) \leq T_h\ then\ f_a^j \\ else\ f_s^i \end{array}\right\} \tag{3.20}$$

where f_s^i and f_a^j denote the i^{th} sensor and j^{th} actuator faults respectively. Based on equation (3.20) a sensor fault is declared if just the angle between the GPV and SP^i is smaller than a threshold value. Conversely, an actuator fault is announced if both the angles between the GPV and SP^i and the GPV and B_n^j are smaller than T_h.

For some cases when B_n^j is inside the cone sector, depending on the dynamics of the system, a sensor fault may produce a GPV aligned with the j^{th} actuator reference direction. This condition makes the sensor fault isolation incorrect, since the j^{th} actuator will be the one declared faulty, according with the logic in equation (3.20). Although it was already proved in equation (3.17) that the the actuator reference direction can not be taken out of sensor reference plane, it is still possible to ensure that the j^{th} actuator reference direction is not aligned with the sensor fault steady-state GPV. This is achieved by adding an optimization constraint during the T_r calculation, as presented in section 4.3.

3.5 Disturbance decoupling

In real world processes there are many disturbances acting on the plant. However, the objective is that the FDI technique presented should be unaffected by such disturbances. Since many disturbances in real plants are accessible, these measured disturbances can be used to decouple their effect from the FDI. This is implemented by introducing them as extra inputs to the FDI technique, by extending the B matrix, the inputs and the left coprime factor $\tilde{N}$ accordingly.

Disturbances are considered to be measurable extra inputs acting on the plant, assuming no particular temporal behavior [6]. The distinction between a disturbance and certain additive faults is indeed subjective. Faults are modelled as additive inputs at particular sensors and actuators, and may specify temporal behavior (e.g., bias faults); any other extra inputs are categorized as disturbances. It is desirable that the FDI approach not be affected by such extra inputs.

In order to demonstrate that residual directionality can be unaffected by extra inputs whose measurements are available, equation (2.7) is rewritten as follows:

$$\dot{x}(t) = Ax(t) + \tilde{B}\tilde{u}(t) \tag{3.21}$$

where $\tilde{B} = [\, B \quad G \,]$, $\tilde{u} = [\, u \quad d \,]^T$, and G and d represent the disturbance allocation matrix and inputs respectively. Using equation (3.21), the coprime factorization definition given by equation (2.19) can be rephrased as:

$$\tilde{N} = C(sI - \tilde{A}_o)^{-1}(\tilde{B} - FE) + E \tag{3.22}$$

Using the modified definition of $\tilde{N}$ given by equation (3.22) and the extended input $\tilde{u}$, disturbance decoupling is implemented in the stable factorization framework to make the GPV immune to disturbance effects.

Chapter 4

Transformation Matrix Optimization

4.1 Introduction

Fault detection and isolation based on the stable coprime factorization approach assures that the parity relations obtained involve stable, proper and rational transfer functions even for unstable plants. Therefore the realizability and stability of the residual generator is guaranteed. However, FDI based on the GPV approach using directional residuals is highly dependent on the dynamics of the system. This means that for some cases, the reference directions may be close or identical, making the isolation for some faults difficult or unachievable. To overcome this situation, the calculation of an optimal transformation matrix T_r is presented in this chapter.

4.2 Problem definition

The transformation matrix T_r in equation (2.25) is an important factor in FDI using directional residuals. Its significance is based on its ability to change the original set of

reference directions to a new one, with better features to improve FDI robustness. The calculated T_r should be able to transform the original system in such a way, that the GPV magnitude ($|GPV|$) after a fault exhibits a significant magnitude change. This requirement assures a clear fault detection. Furthermore, T_r should provide enough separation between the reference directions and planes, guaranteeing an unambiguous fault isolation despite nonlinear effects and modelling uncertainty.

In most cases it is required to compute a transformation matrix ($T_r \neq I_{n\times n}$). This need is evidenced in the following results obtained for the JCSTR model. First, a -50% bias heating fluid inflow valve fault is applied at *t=5 hours* for a temperature setpoint variation of +3% and a volume setpoint variation of +7% at t=0, as shown in the figures below.

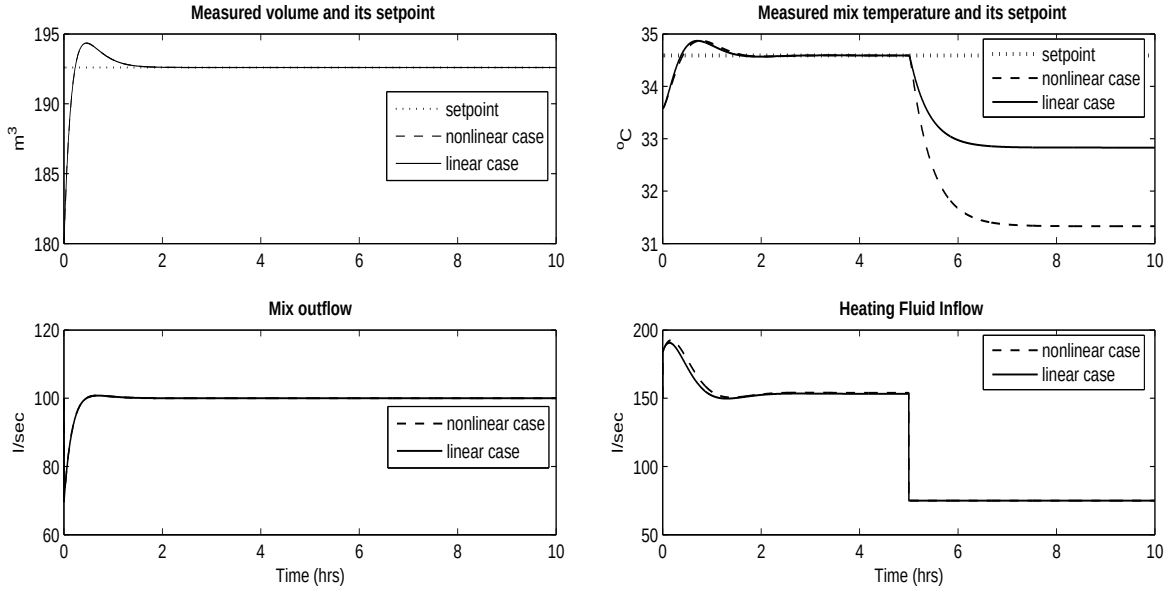

(a) (b)

Figure 4.1: Time histories for a -50% bias heating fluid inflow valve fault

Figure 4.1(a) shows the volume sensor and the mix outflow time histories. Since the volume only depends on the fluid inflow and outflow valve actions, this is not affected by the heating fluid inflow valve failure. In Fig. 4.1(b) is observed the effect that this fault has in the heating fluid inflow and the temperature behavior. In Fig. 4.2(a) we observe a significant increment in the GPV magnitude, allowing us to detect the failure right away. However, isolation is difficult since the angles between the GPV and the volume sensor reference plane, and the GPV and the outflow and heating inflow valves reference directions, are all close to zero as shown in Fig. 4.2(b).

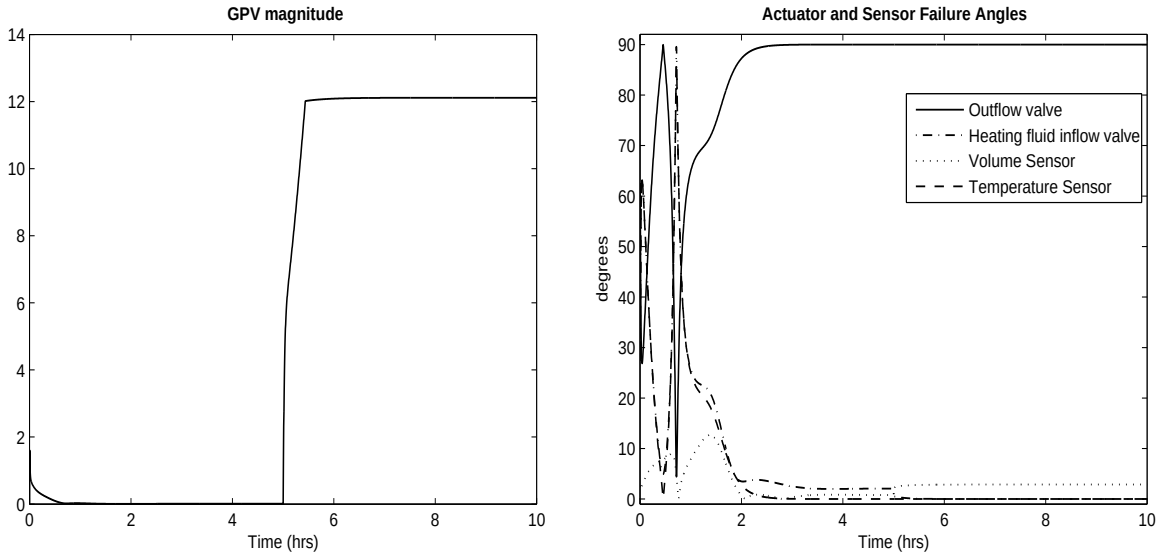

(a) (b)

Figure 4.2: GPV behaviour for a -50% bias heating fluid inflow valve fault

The isolation problem is due to the dynamics of the system which does not provide a well separated set of reference planes and directions. This fact is better demonstrated in table 4.1 which includes the angles between the different actuator reference directions and sensor reference planes. In this table is shown that the angle between

$\measuredangle$ (°)	B_n^{ov}	B_n^{hv}
B_n^{ov}	-	90
B_n^{hv}	90	-
SP^v	0	2.86
SP^t	90	0

Table 4.1: Untransformed reference directions angles

B_n^{ov} and SP^v is zero, which means that the outflow valve reference direction lies on the volume sensor reference plane. The same condition is presented between the heating fluid inflow valve and the temperature sensor. This situation corresponds to the special case for actuator FDI illustrated previously in Fig. 3.3 and defined by equation (3.16), and is treated as described. It is also observed that the angle between SP^v and B_n^{hv} is equal to 2.86°. Since this separation angle is very small, the isolation is difficult because the GPV will be close to or lie on more than one reference plane or direction. This situation can be solved by transforming the original system using a suitable T_r that improves its FDI capabilities. The transformation matrix computation is presented in the following section.

4.3 Transformation matrix computation

It is desirable to choose T_r to increase the separation angle between the original set of reference directions as much as possible, to enhance robustness and maximize the number of faults that can be isolated and the number of disturbances that can be decoupled, beyond the number of outputs of the system [7].

This can be formulated as a constrained optimization problem, whose objective is to maximize the angles between the transformed reference directions, to the extent possible. The optimization routine maximizes the minimum of $F_{i,j}(T_r)$, where $F_{i,j}(T_r)$ is the objective function containing the angles between the reference directions that are separable [13]. This is implemented by minimizing $-F_{i,j}(T_r)$, using the *fminimax* function in the MATLAB® optimization toolbox, which uses a sequential quadratic programming (SQP) method. This method solves the constrained optimization problem in a similar way as Newton's method for unconstrained optimization. An approximation of the Hessian of the Lagrangian function is made at each major iteration, using a quasi-Newton updating method. This result is used to generate a QP subproblem whose solution is used to form a search direction for a line search procedure.

In this context, the term "separable" refers to those directions which do not satisfy equation (3.17). The angle between those actuator reference directions which are lying on one of the sensor reference planes, should be excluded from the $F_{i,j}(T_r)$ function, since it was already proven that it is not possible to calculate a T_r to separate them. By determining this special case, the optimization performance is improved. The mathematical formulation is given by:

$$F_{i,j}(T_r) = \measuredangle(Z_i, Z_j) \tag{4.1}$$

$$\max_{T_r} \min_{\{F_{i,j}\}} \{F_{i,j}(T_r)\} \tag{4.2}$$

$$\textit{such that } c(T_r) \leq 0\ ,\ c_{eq}(T_r) = 0$$

where $c(T_r) \leq 0$, $c_{eq}(T_r) = 0$ represent nonlinear inequality and equality constraints, respectively; and Z_i and Z_j are transformed reference directions. These directions

are given by transforming B_n^j, B_d^i and E_d^i.

4.3.1 Nonlinear optimization constraints

The T_r calculation approach proposed using optimization is highly flexible. It allows adding different nonlinear constraints to take into account the dynamics of the system. In order to refine the optimization problem the following three nonlinear constraints of the form $c(T_r)$ and $c_{eq}(T_r)$ are implemented.

1. A compulsory constraint is imposed on $Cond(T_r)$, the condition number of T_r; $Cond(T_r) \leq C_{max}$ improves the stability and robustness of the FDI response. C_{max} depends on the application and should be the smallest possible that allows the optimization routine to converge to a solution. Specifically, by constraining $Cond(T_r)$, one obtains smoother behavior of the GPV angles and smaller fault-free $|GPV|$ during transients. These features are highly desired to enhance the FDI performance. If the transformation matrix is calculated without using this constraint, it most probably results in an ill-conditioned T_r which yields poor results for the optimization routine.

2. An optional constraint normalizing T_r is applied; $|T_r| = 1$ normalizes the transformed parity vector.

3. A case dependent constraint on the $\measuredangle(GPV_{ss}^i, Z_j)$ may be required if the system dynamics lead to the special case defined by equation (3.16). The actuator FDI issue is overcome by implementing the logic presented in equation (3.20), which

is only effective if the j^{th} actuator direction vector which lies on the plane SP^i is outside the cone defined by vectors B_s^i and E_d^i. Figures 4.3 and 4.4 illustrate how these sensor fault sectors are defined for the JCSTR model and their relations with B_n^j.

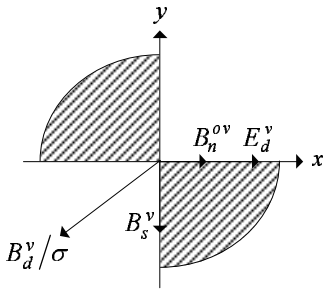

Figure 4.3: Volume sensor fault sector

In Fig. 4.3 it is observed that the outflow valve reference direction B_n^{ov} lies on the boundary of the volume sensor fault sector, making isolation difficult. Ideally, isolation based on the steady-state GPV activity along B_s^v should still be feasible. However, this is only true for the pure linear case and when there is not a high

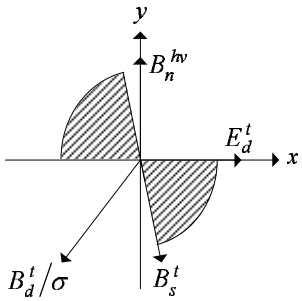

Figure 4.4: Temperature sensor fault sector

interaction between the variables. Conversely, in Fig. 4.4 the heating inflow valve reference direction B_n^{hv} is well outside of the temperature sensor fault sector, which is desirable for the sensor fault isolation. For the case shown in Fig. 4.4 we may want to maximize the angular separation between B_n^{hv} and the cone, in the situation depicted in Fig. 4.3 we can maximize the angle between B_n^{ov} and B_s^v if the steady state strategy is used.

To overcome the FDI ambiguity arising from the sensor-actuator special case defined in section 3.4 when B_n^j is inside the cone sector, an additional constraint is required. This assures a minimum separation angle between the steady-state GPV for the i^{th} sensor and the j^{th} actuator reference direction to be large enough to provide an unambiguous isolation. This can be expressed mathematically as:

$$\measuredangle(GPV_{ss}^i, Z_j) \geq \Theta_{min} \tag{4.3}$$

where Θ_{min} should be the largest angle possible that allows the optimization routine to converge to a solution. If this constraint is omitted during the optimization routine, there is no guarantee that the resulting T_r will provide enough separation to distinguish the i^{th} sensor fault from the j^{th} actuator fault, for systems satisfying equation (3.16).

Chapter 5

Decision Maker

5.1 Introduction

Once the residuals are generated, a decision maker block is implemented to interpret the magnitude and angle changes to make an FDI diagnosis. These results are sent to the supervisory system, which displays the corresponding fault alarms through the human interface. In most real world processes the operating point is continuously changing, and this becomes an issue for model-based FDI techniques [16], applied to nonlinear plants. This topic is analyzed in detail in section 6.1. To overcome this situation, the modeling errors must be taken into account by implementing an adaptive decision maker block [3].

The decision maker is composed of both the detection and isolation blocks, as shown in Fig. 5.1. After the residual generator block executes, the GPV magnitude ($|GPV|$) and the different GPV angles ($\angle GPV_k$) are available to perform the detection and isolation, respectively. If the $|GPV|$ exceeds the magnitude threshold, a fault is detected and the isolation block is executed. Otherwise, the FDI algorithm declares

normal operation. These blocks are described in detail in the following sections.

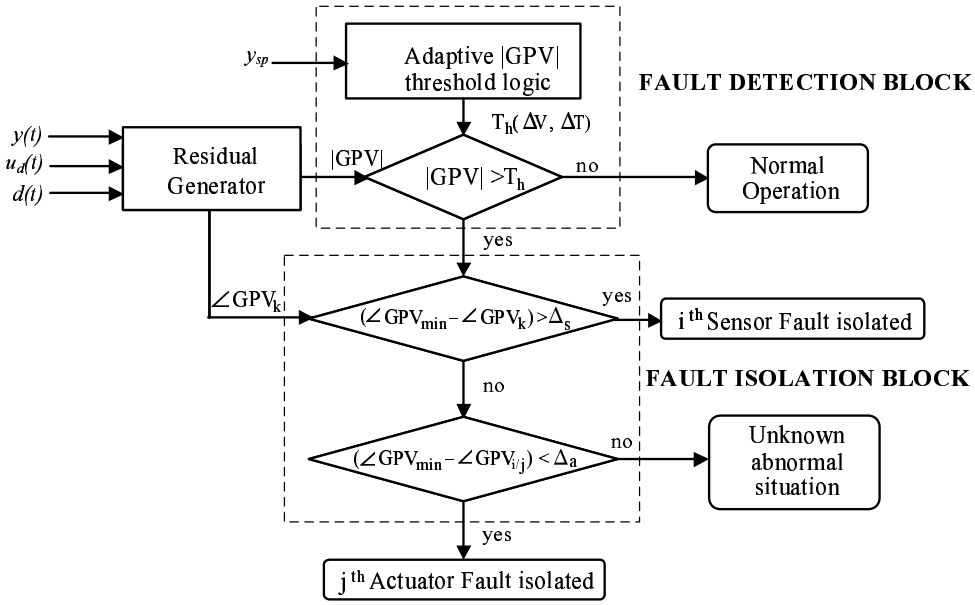

Figure 5.1: Decision maker block diagram

5.2 Detection block

It is assumed that the process is under closed-loop control, and the control system inputs are output setpoints, y_{sp}. The detection block is implemented using an adaptive $|GPV|$ threshold logic. This threshold logic uses y_{sp} as input and provides a threshold value depending on the setpoint variations. Since the detection using the GPV technique is based on the magnitude increment with respect to the fault free GPV magnitude, $|GPV|_{ff}$, the threshold was calculated based on the $|GPV|_{ff}$ at each operating point. If a good estimate of the $|GPV|_{ff}$ is available, the threshold value

can be defined as $K \times |GPV|_{ff}$, where $K > 1$ depends on the system. The value of K regulates the tradeoff between detection speed and the occurrence of false alarms. If K is too small, it may generate false alarms due to the $|GPV|_{ff}$ estimation errors. Conversely, if K is very large, the detection may be too slow or impossible for small or even medium size faults. For the JCSTR study, a value of K=2.5 provided a good tradeoff, yielding low false alarm and misdetection rates along the controller envelope defined in section 6.1. However, this application required knowledge of $|GPV|_{ff}$ at different operating points, y_{sp}.

Four different techniques were used to estimate the $|GPV|_{ff}$ for each setpoint variation inside the operating envelope. First an empirical threshold scheduled logic was attempted, followed by piece-wise linear, quadratic and cubic threshold function fitting. Each of the techniques' strengths and weaknesses are illustrated in section 7.4.

5.2.1 Empirical threshold scheduled logic

A fixed threshold was not a viable implementation for the JCSTR because of non-linearity, as analyzed in chapter 6. The first attempt to overcome this issue was to implement an empirical scheduled threshold logic. For this method, the $|GPV|_{ff}$ values were determined by simulations for different setpoint variations ΔV and ΔT within the controller envelope. Using these values, different threshold regions were defined for those setpoint variations for which the $|GPV|_{ff}$ did not change significantly. For each region, the $|GPV|_{ff}$ average was calculated and stored as a single fault free $|GPV|$ for the whole area. When a setpoint variation is applied, the threshold region

to which it belongs is identified and its corresponding $|GPV|_{ff}$ average is used to set up the threshold value as $T_h = K \times |GPV|_{ff}$.

The advantage of this method is its ability to take into account highly nonlinear $|GPV|_{ff}$ variations. However, this may only be effective if many threshold regions are defined, which is impractical and time consuming, due to the large data base required to store the average $|GPV|_{ff}$ for each region.

5.2.2 Piece-wise linear threshold logic

In order to overcome the limitations presented in the previous method, a piece-wise linear threshold logic was developed. To implement this method the $|GPV|_{ff}$ and the $|GPV|$ for a -20% fault was determined for a few ΔV and ΔT values inside the controller envelope. A fault size of -20% was chosen for this study for having small $|GPV|_{faulty}$, which makes the detection more challenging. As the fault size increases, the $|GPV|_{faulty}$ increases, which is desirable for detection. Therefore, if the threshold logic is able to detect -20% size faults, it guarantees correct detection for fault sizes with larger $|GPV|_{faulty}$. These results together with their estimated threshold are displayed in Fig. 5.2 and 5.3.

The estimated thresholds are functions only of ΔV or ΔT, since in each figure we are considering the variation of only one setpoint at a time. These estimated thresholds were calculated as $0.5 \times (|GPV|_{ff} + |GPV|_{min})$ to guarantee an unambiguous isolation in the worst case. In this equation, $|GPV|_{min}$ corresponds to the smallest $|GPV|$ in Fig. 5.2 and 5.3. Using the estimated threshold for ΔV=0 and ΔT=0, the

3D piece-wise linear threshold is given by:

$$T_h = T_h^0 + K_V \Delta V + K_T \Delta T \tag{5.1}$$

where T_h^0 is the threshold value at the nominal operating point in Fig. 5.2 and 5.3.

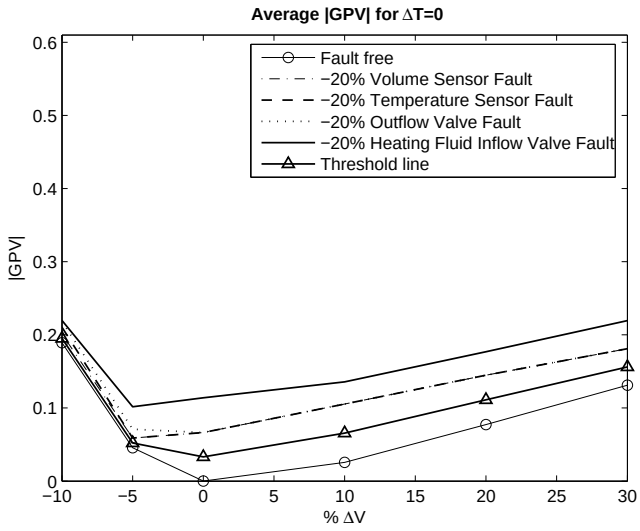

Figure 5.2: Average $|GPV|$ for ΔT=0

The volume and temperature slopes, K_V and K_T, are calculated from the estimated threshold plotted in figures 5.2 and 5.3 respectively, considering three regions: Δ<-5%, -5%<Δ<0% and Δ>0%. According with the region where ΔV and ΔT lie, the slopes are selected and the threshold value is calculated using equation (5.1). Fig. 5.4 shows the 3D piece-wise linear obtained for the controller envelope.

The piece-wise linear threshold method is more efficient to implement and less time consuming than the logic proposed in section 5.2.1. It is also more accurate since it adapts the threshold at each operating point instead of scheduling a fixed

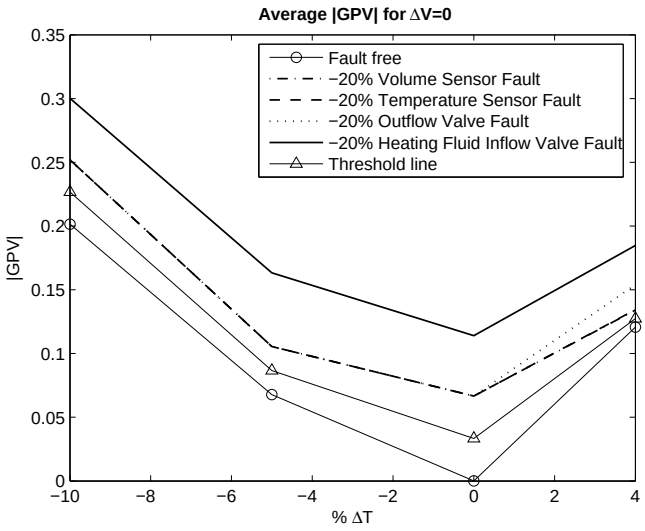

Figure 5.3: Average $|GPV|$ for ΔV=0

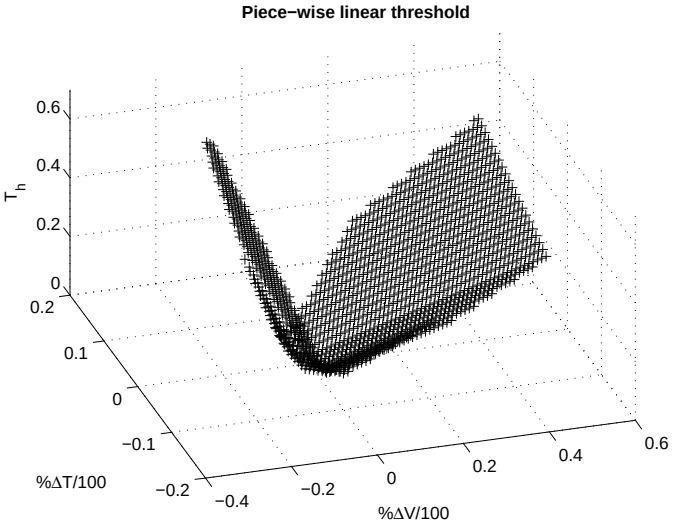

Figure 5.4: 3D Piece-wise linear threshold

one for a whole region. However, since the relation between the $|GPV|_{ff}$ and the operating point is indeed nonlinear, this approximation fails for a few regions with high nonlinear behavior.

5.2.3 Quadratic threshold logic

The quadratic logic was implemented to provide an adaptive threshold capable of taking into account the nonlinear relation between the $|GPV|_{ff}$ and the operating point. First the $|GPV|_{ff}$ was obtained for 361 different setpoint variations along the controller envelope. Using these values a surface-fit was performed using a free trial demo of TableCurv 3D V4.0 ©SYSTAT Software Inc. The obtained fitting has the quadratic form $z = a + bx + cy + dx^2 + ey^2 + fxy$, that was rewritten in terms of the variables to provide the following equation for the $|GPV|_{ff}$:

$$|GPV|_{ff} = a + b\Delta V + c\Delta T + d\Delta V^2 + e\Delta T^2 + f\Delta V\Delta T \tag{5.2}$$

Using equation 5.2 the adaptive threshold is defined as $T_h = K \times |GPV|_{ff}$ with *K=2.5*. The polynomial coefficients and the different statistical parameters describing equation 5.2 are attached in appendix B.1. Fig. 5.5 illustrates the surface-fit for the controller envelope showing the nonlinear relation between the operating point and the $|GPV|_{ff}$.

The quadratic threshold logic is more efficient and accurate than the previous ones, providing better $|GPV|_{ff}$ estimates even for the highly nonlinear regions. However, since the coefficient of determination r^2 is only 0.65, there will be still some highly nonlinear regions for which the fitting may be inaccurate.

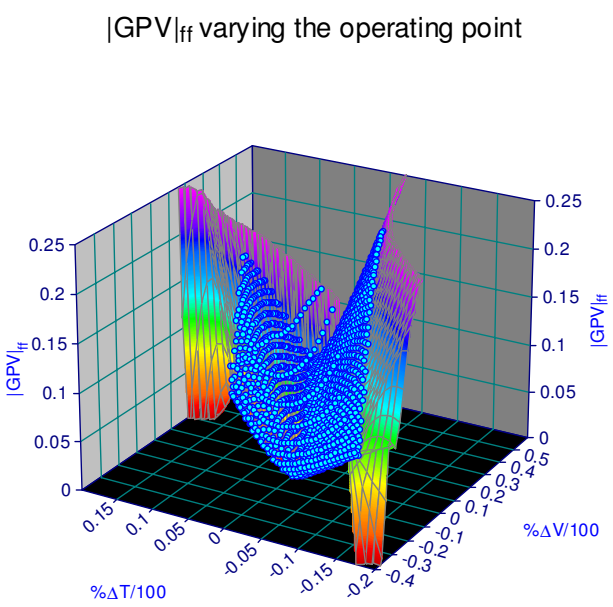

Figure 5.5: $|GPV|_{ff}$ Quadratic fitting

5.2.4 Cubic threshold logic

A cubic threshold logic was implemented to increase the accuracy of the $|GPV|_{ff}$ estimate. The same procedure used in the quadratic threshold was implemented using TableCurv 3D, but the resulting fitting was a bivariate cubic polynomial of the form $z = a + bx + cy + dx^2 + ey^2 + fxy + gx^3 + hy^3 + ixy^2 + jx^2y$. By rewriting this equation in terms of the variables, the $|GPV|_{ff}$ is defined as:

$$\begin{aligned} |GPV|_{ff} &= a + b\Delta V + c\Delta T + d\Delta V^2 + e\Delta T^2 + f\Delta V\Delta T + \\ &\quad g\Delta V^3 + h\Delta T^3 + i\Delta V\Delta T^2 + j\Delta V^2\Delta T \end{aligned} \tag{5.3}$$

The polynomial coefficients and the different statistical parameters describing equation 5.3 are attached in appendix B.2. Figure5.6 illustrates the surface-fit for the

controller envelope, described by equation (5.3).

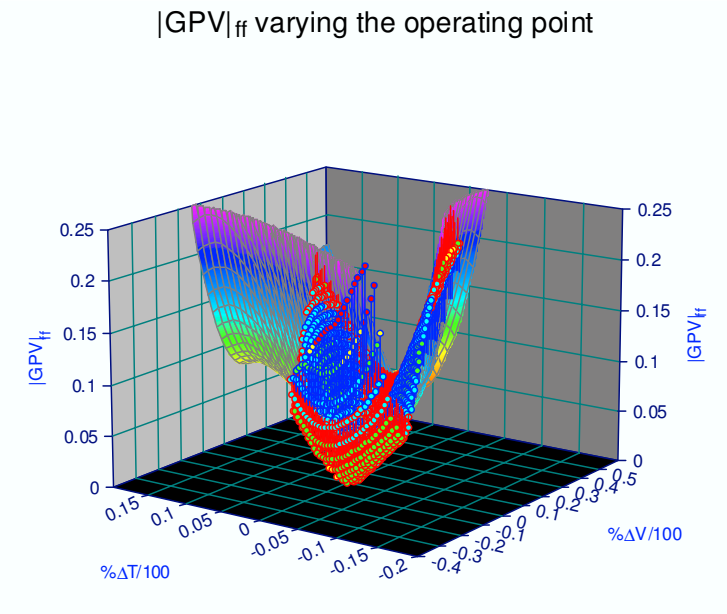

Figure 5.6: $|GPV|_{ff}$ Cubic fitting

The cubic threshold logic significantly improves the efficiency with respect to the empirical scheduled and the piece-wise threshold logics. However, the enhancement with respect to the quadratic approach is just slight, even though the coefficient of determination r^2 increases from 0.65 to 0.85. This improvement is only noticeable for a few operating points, but it does not make a significant difference in most of the highly nonlinear regions. This is discussed further in section 7.4 by comparing the performance of the four different techniques in the JCSTR application.

5.3 Isolation block

The isolation block identifies which fault was detected using the logic depicted in Fig. 5.1. Since we are not considering concurrent faults (assuming they are unlikely to happen), the isolation block is simplified using $\angle GPV_{min}$, which is defined in equation (5.5). This avoids the issue of estimating an angle threshold to determine which angles are close to zero.

$$\angle GPV_k(\theta) = \measuredangle(GPV_{ss}\,, Z_k) \tag{5.4}$$

$$\angle GPV_{min} = \min_{\theta} \angle GPV_k(\theta) \tag{5.5}$$

Once the detection block is executed, the angle between the GPV and each reference direction and plane is calculated. Then, the differences between the smallest GPV angle ($\angle GPV_{min}$) and the rest are computed and compared with the sensor angle threshold Δ_s. If all the differences are larger than Δ_s, a fault in the k^{th} sensor is identified, where k represents the sensor with the minimum angle. This logic ensures that the separation between the minimum angle and the rest is large enough to isolate the fault unambiguously.

In the JCSTR model both actuators satisfy equation (3.16) and therefore their isolation qualifies as the special case described in section 3.4. Based on this fact, it is valid to state at the first stage that the fault corresponds specifically to a sensor case. This is because for the actuator cases the GPV angle will lie not only in the corresponding actuator reference direction, but also on a sensor reference plane. Therefore, if the Δ_s is exceeded, it means that the GPV was not exhibiting this situation. On

the contrary, if Δ_s is not exceeded, the difference between the $\angle GPV_{min}$ and its corresponding actuator or sensor pair that satisfies equation (3.16) is calculated. If it is less than the actuator angle threshold Δ_a a fault in the corresponding actuator is isolated. Otherwise, an unknown abnormal situation is declared. The unknown abnormal situation represents a case when the separation angle between the $\angle GPV_{min}$ and the others is not large enough and does not satisfy the actuator isolation logic. Even though the FDI is ambiguous for this situation, the algorithm is still capable of displaying an unknown abnormal situation, avoiding a missed alarm.

Chapter 6

Robustness Analysis

6.1 Operating point variability

In most real world plants, the operating point is continuously changing in order to satisfy production requirements. Although the large-signal behaviour of an actual process is indeed nonlinear, most of them are controlled using a linear-based algorithm designed for small deviations around a nominal operating point. Since large setpoint variations will result in significant deviations from the nominal linearized model, they may yield a poor approximation of the nonlinear model at this new operating point and therefore poor controller performance. Since the Generalized Parity Vector (GPV) technique is also a linear model-based approach, the modelling error becomes a significant issue for FDI robustness as well.

In order to analyze the robustness with respect to modelling errors in a realistic framework, we first determine the envelope where the controllers for both the linear and nonlinear models work properly. The control objective was taken to be zero steady state error, so the proportional plus integral (PI) algorithm was used. The inside of

this envelope is defined to consist of those operating points where the system does not show a steady state error. The crossed area shown in Fig. 6.1 indicates the region where the plant is properly controlled using both the linear and the nonlinear model. Conversely, the dotted section is the area where either one or both controllers exhibit steady state error due to the highly nonlinear behavior of the process. Hereinafter the crossed area will be called the controller envelope and will be the operating region of interest to test the FDI performance.

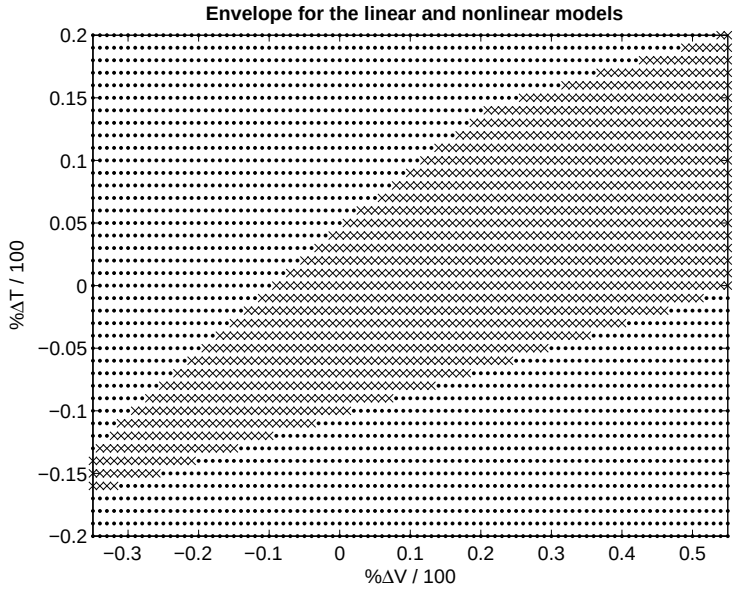

Figure 6.1: Envelope for the linear and nonlinear controller

To estimate the FDI performance inside the controller envelope, a fault size of -50% was applied for each sensor and actuator for 361 different setpoints variations. For each ΔV and ΔT the FDI results were evaluated for each fault and plotted in the corresponding figure, according with the plot symbols describe in table 6.1.

PLOT SYMBOL	FDI PERFORMANCE
o	Fast and sure
$\triangle$	Fast but short
$+$	Slow but sure
$\square$	Ambiguous
$*$	Only detection
$\times$	FDI not possible

Table 6.1: FDI envelope plot symbols

6.1.1 Volume sensor FDI envelope

Figure 6.2 illustrates the FDI performance within the controller envelope for a -50% volume sensor fault. It is observed that most of the time, the FDI algorithm yields circle markers, which characterize the ideal case, where the fault is detected right away and the isolation period is long. A small area defined by triangles represents the region where the fault is detected right away as well, but the isolation period is short. This situation is due to the nonlinear interaction that the volume has on the temperature as stated in equation A.2, appendix A. Thus, when a volume sensor fault is applied at some operating points, the temperature loop is significantly disturbed after some minutes affecting the residual directionality. However, the performance of the FDI is still acceptable since it provides a clear isolation period of around 15 minutes strengthened by a subsequent "unknown abnormal situation" alarm.

Finally, there are two small areas represented by squares, which represents an ambiguous isolation. In this case, the volume sensor fault is detected for a short

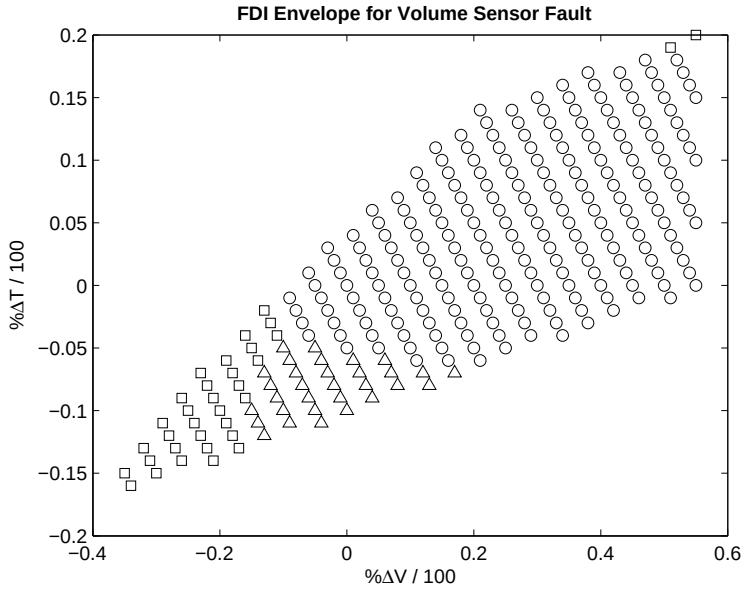

Figure 6.2: FDI Envelope for volume sensor fault

period of time, preceded or followed by an outflow valve fault alarm. This situation is due to a special case for sensor-actuator faults described in section 3.4. To overcome this situation, a constraint was added during the T_r calculation to ensure that the outflow valve reference direction was not aligned with the sensor fault steady-state GPV. However, its validity is limited to a region surrounded the nominal operating point, due to the nonlinearities involved. This is evidenced in figure 6.2, since the ambiguous FDI region starts for values of ΔV < -10%. Even though it is undesirable for FDI, it is still within the expected limitations for this method since designs based on linearized models are generally supposed to be valid for ±10% setpoint variations around the nominal operating point.

6.1.2 Temperature sensor FDI envelope

Figure 6.3 shows the FDI performance for the controller envelope when a -50% temperature sensor fault is applied. It is observed that the GPV technique is able to isolate the fault clearly for all setpoint variations inside the envelope. Even for large setpoint variations, the detection was fast and the isolation period was extensive and unambiguous, which is highly desirable for FDI. These features were enhanced by transforming the original system using the T_r calculation method presented in chapter 4.

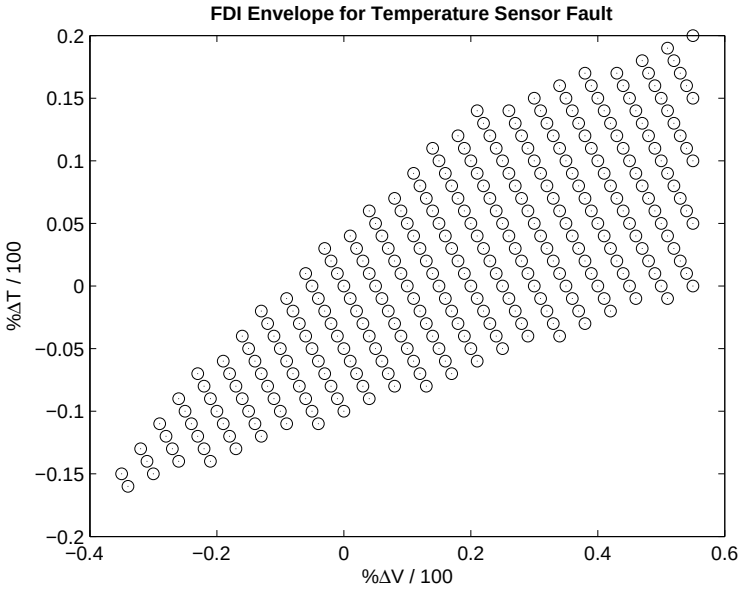

Figure 6.3: FDI Envelope for temperature sensor fault

6.1.3 Outflow valve FDI envelope

Figure 6.4 illustrates the FDI performance along the controller envelope for a -50% outflow valve fault. It can be observed that for this fault case, the FDI shows a variety of performance regions. This is due to the fact that the outflow valve controls the mixture volume and, as a result, it affects the temperature of the mixture as well. This is evidenced in the dominant region defined by triangles, that characterizes a fast but short FDI response. In this area the detection was fast, but the isolation period was no more than 15 minutes, as a consequence of the nonlinear behavior of the temperature. Nevertheless, the FDI performance is satisfactory since it provides a clear isolation period of around 15 minutes, strengthened by a subsequent unknown abnormal situation alarm.

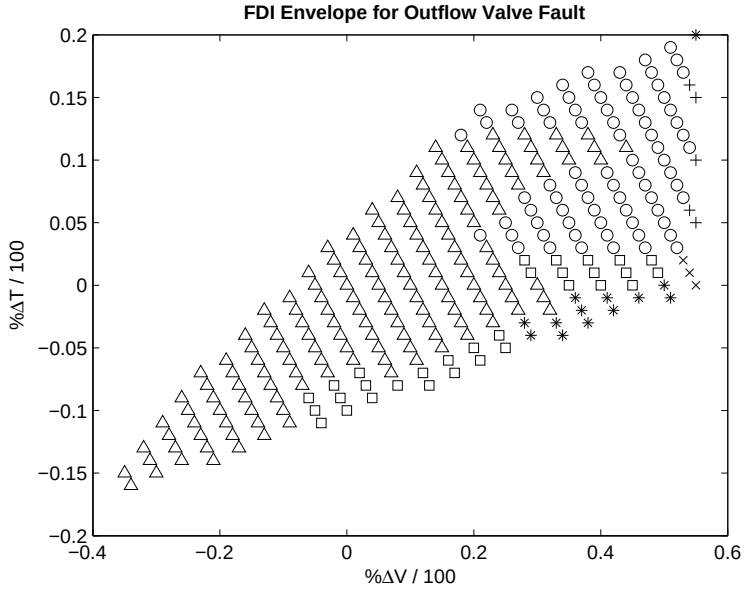

Figure 6.4: FDI Envelope for outflow valve fault

The second largest region is defined by circles, which represents the ideal case where the fault is detected immediately and the isolation period is long. This region is characterized for large volume setpoint variations, which is advantageous because those setpoint values are close to the saturation level (maximum capacity of the tank). Hence, when the outflow valve fault is applied, the effect in the volume is not significant and therefore the nonlinear effect on the temperature is not remarkable. As a result of this, the GPV is not lying close to the temperature reference plane, even a long time following the fault.

The third region is depicted by squares, which represents an ambiguous isolation. In this region either the volume or temperature setpoint variations are large, which accentuates modeling errors. Because of this, the residual directionality is affected as the GPV points towards the outflow valve reference direction only for a very short period of time (less than 5 minutes) and later it points towards the heating fluid inflow valve reference direction. Since the clear isolation period is not long enough and it is followed by a heating fluid inflow valve fault alarm, the FDI is declared ambiguous. Although this is an undesirable situation for FDI it is not that critical since most of the ambiguous cases are near the envelope boundary or presented for $\Delta V > 20\%$ which are outside the $\pm 10\%$ expected functioning range for the linearized model.

The small region symbolized by asterisks represents setpoint variations where only detection is possible. For these setpoints, the nonlinear effect in the temperature becomes more remarkable and therefore the GPV directionality is significantly affected.

However, the FDI algorithm is still capable of providing a prolonged "unknown abnormal situation" signal, avoiding false alarms but detecting an irregular condition in the system.

There are a few cases denoted by crosses where the fault is detected after a while, but the isolation period is extended and clear. These cases are for some $\Delta V > 54\%$, variations for which the setpoint values are very close to the saturation level. Hence, if the outflow valve is stuck, the effect on the volume level is not significant because it cannot increase beyond the maximum capacity of the tank. As a result, it will take a longer time for the GPV to be significantly affected by this fault and this will delay the detection, by as much as 20 minutes.

Finally, there were just 3 cases defined by x's where the FDI did not work. These cases were for some $\Delta V > 53\%$ where the modeling errors became extreme, yielding a large fault free GPV magnitude. Because of the large $|GPV|_{ff}$, the magnitude increment after the fault is not large enough to be detected by any of the detection logics proposed in section 5.2. However, this situation is not a critical issue for the JCSTR FDI system, since it is present only for three setpoint values (over 361 tested) and these were located on the corner of the envelope boundary. The plant is unlikely to operate in this region.

6.1.4 Heating fluid inflow valve FDI envelope

Figure 6.5 shows the FDI performance for the controller envelope when a -50% heating fluid inflow valve fault is applied. It was verified that the FDI algorithm is capable of

unambiguously isolating the fault for all the setpoint variations inside the envelope. For significant setpoint variations, the detection was quick and the isolation period was large and definite. The isolation features were improved by the proper calculation of the transformation matrix, allowing it to increase the separation angle between the volume sensor reference plane and the heating fluid inflow valve reference direction from 2.86° to 56.94°.

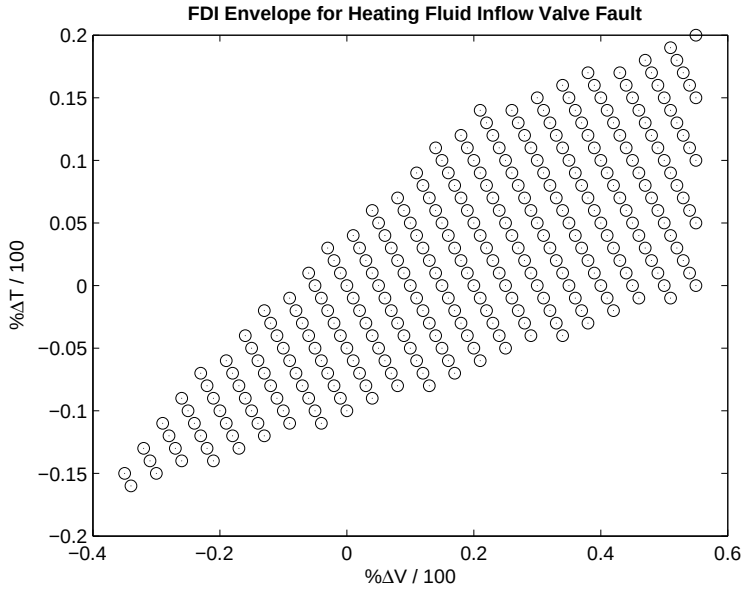

Figure 6.5: FDI Envelope for heating fluid inflow valve fault

6.2 Fault size analysis

In order to test the robustness of the GPV technique with respect to the fault size, different scenarios for each type of fault were simulated at the nominal operating

point. The minimum fault size was set at ±10%, since we are not interested in detecting smaller faults. For the actuator case, the fault size defines the % with respect to the steady state value at which the valve is stuck. For the sensor case, it determines the bias with respect to the actual value. The results for different negative and positive fault sizes are tabulated in tables 6.3 and 6.4 respectively, using the notation presented in table 6.2.

SYMBOL	**FDI PERFORMANCE**
o	Fast and sure
△	Fast but short

Table 6.2: Symbols for fault size analysis

It was verified from the simulations that the faulty GPV magnitude increases with the fault size, as expected. This occurs because the difference between the analytically computed and the sensory measurement values is more significant when the latter is perturbed for larger faults. Although the value of the faulty GPV magnitude changes considerably for each fault type and size, the GPV technique was able to detect and isolate the fault properly for the scenarios symbolized by a **o** in tables 6.3 and 6.4. This is a result of the implemented detection logic described in section 5.2.

Most of the volume sensor fault cases are labelled with a △ which represents fast detection with a short isolation period. This is because the volume control loop is able to reject the fault quickly, driving the measured mixture level back to the setpoint and the mix outflow to the nominal steady state. Since these are the only

measurements affecting the volume parity equation, the GPV will point towards the volume reference direction only for a short period of time while the fault has not been rejected. However, since the actual mixture level inside the tank is different than the measured one (due to the sensor fault), this will affect the measured temperature and heating fluid inflow. As a consequence of this, the FDI algorithm is still able to detect an unknown abnormal situation even after the fault is rejected. Conversely, when a negative volume sensor fault $\geq 50\%$ is applied, the volume loop is not able to reject it and therefore the isolation period is extended.

These results demonstrate that the performance of the GPV technique is not restricted by the fault size. On the contrary, as the fault size increases, its performance improves showing a faster detection and more definite isolation, while being sensitive enough to detect small size faults.

FAULT SIZE / FAULT TYPE	-10%	-20%	-30%	-40%	-50%	-60%...	-80%	-100%
Volume Sensor	△	△	△	△	o	o	o	o
Temperature Sensor	o	o	o	o	o	o	o	o
Outflow Valve	o	o	o	o	o	o	o	o
Heating Fluid Inflow Valve	o	o	o	o	o	o	o	o

Table 6.3: Negative fault size robustness analysis

FAULT SIZE / FAULT TYPE	10%	20%	30%	40%	50%	60%...	80%	100%
Volume Sensor	△	△	△	△	△	△	△	△
Temperature Sensor	o	o	o	o	o	o	o	o
Outflow Valve	o	o	o	o	o	o	o	o
Heating Fluid Inflow Valve	o	o	o	o	o	o	o	o

Table 6.4: Positive fault size robustness analysis

Chapter 7

Simulation Results

7.1 Introduction

The FDI algorithm was implemented using MATLAB® and applied to a simulated model of the jacketed continuously stirred tank reactor described in appendix A. In order to test the performance in various circumstances presented in the previous chapters, different sensor and actuator faults were applied. Both linear and nonlinear models were used in this study, and time histories for both models are shown in all plots even though they coincided in a number of cases. The conditions given are all with reference to one of the two nominal setpoint specified in appendix A, i.e, $\Delta T = T_{sp} - T_o$, $\Delta V = V_{sp} - V_o$.

7.2 Transformation matrix results

In order to test the performance of the transformation matrix obtained using optimization, several scenarios were simulated to show its effect in the FDI for each constraint separately and all of them together.

To illustrate the effect of constraint 1 (condition number), a -50% bias outflow valve fault is applied at t=5 hours for a temperature setpoint variation of +5% and a volume setpoint variation of +5%. The corresponding time histories are attached in appendix C, Figs. C.1 and C.2.

In figure 7.1, the original set of directions was transformed using a T_r obtained by applying the procedure presented in section 4.3 but eliminating constraint 1. The effect of excluding this constraint is shown in the GPV angle's behavior. It is observed that the outflow valve angle and the volume and temperature sensor angles are all close to zero making the isolation unachievable.

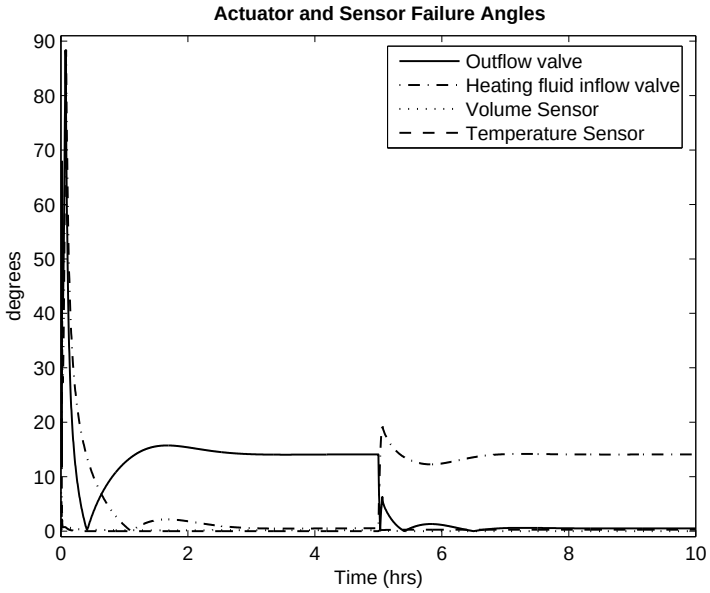

Figure 7.1: $\angle GPV$ without using constraint 1

In contrast, in Fig. 7.2 it is observed that by adding constraint 1, the separation

angle between the temperature sensor angle and the outflow valve and sensor angles increases significantly, allowing a clear isolation by applying the logic given in equation 3.20.

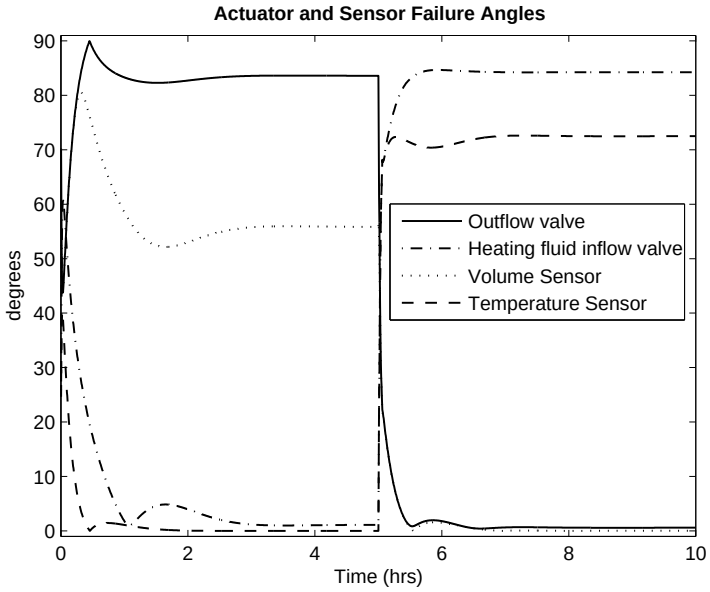

Figure 7.2: $\angle GPV$ using constraint 1

To analyze the effect of constraint 3 (angle condition for the special case), a -50% volume sensor fault is applied for a volume setpoint variation of 7% and a temperature variation of 5%. The corresponding time histories are attached in appendix C, Figs. C.3, C.4, C.5 and C.6. In Fig. 7.3 it is observed that the GPV without constraint 3 is not only lying on the volume sensor reference plane after the fault is applied, but also almost in the outflow valve reference direction. This is evidenced in the fact that both the sensor and outflow valve angles lie close to zero, making the isolation unattainable. However, by adding constraint 3, the separation angle between the volume sensor and

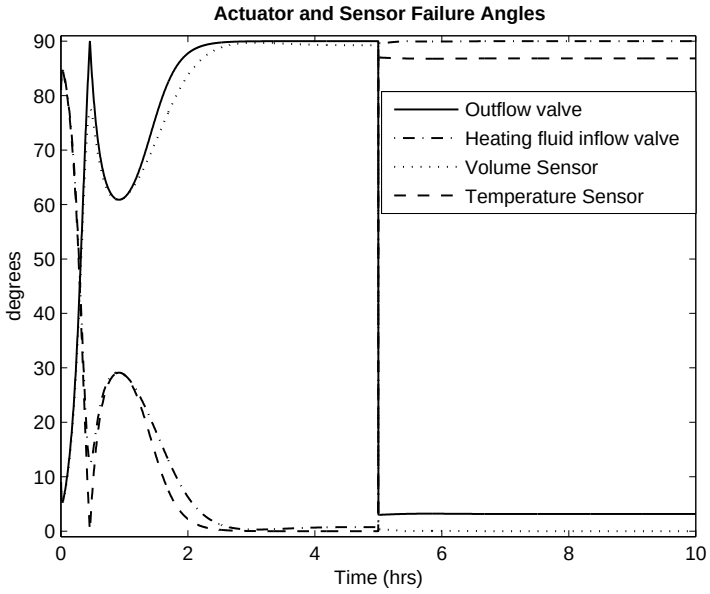

Figure 7.3: $\angle GPV$ without using constraint 3

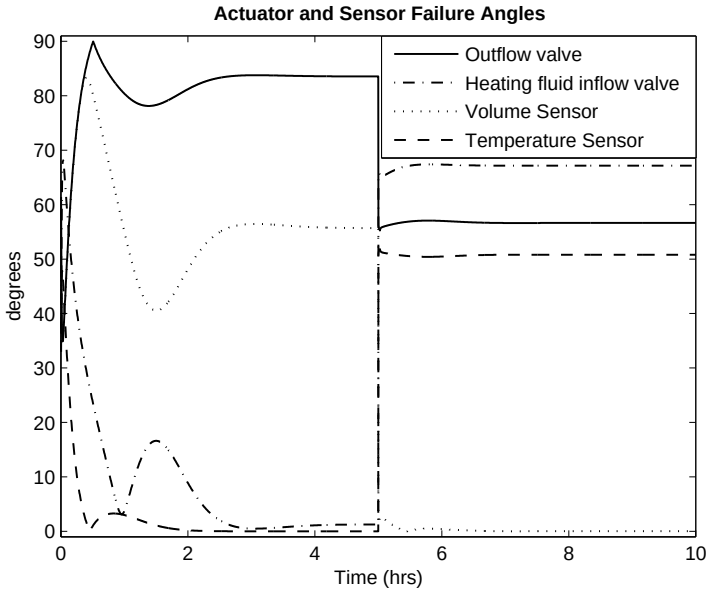

Figure 7.4: $\angle GPV$ using constraint 3

the outflow valve increases significantly allowing a definite isolation as shown in figure 7.4. The corresponding $|GPV|$ with and without using this constraint are are shown in appendix C figures C.7 and C.8 respectively.

Finally, a -50% heating fluid inflow valve fault was applied for a volume setpoint variation of 7% and a temperature variation of 3%. The time histories for this case are illustrated in appendix C, figures C.9, C.10, C.11 and C.12. For this case the system is transformed using a T_r obtained by combining all the previous constraints during its calculation. By comparing figures 7.5(a) and 7.6(a) the effect of constraint 2 ($|T_r| = 1$) can be observed, which is optional since it only affects the $|GPV|$ scale. In figure 7.5(b) it can be seen that the isolation is not possible because the heating fluid inflow valve, the temperature and volume sensor angles are all close to zero. However, by looking at figure 7.6(b) it is observed that for the transformed system, the volume sensor angle lies far enough from the heating fluid inflow valve angle, making the actuator isolation possible by applying the logic in equation 3.20.

This is confirmed in table 7.1 where it is observed that this angle increases from 2.86° to 62.58°, which is large enough to provide a clear isolation. At the same time, the other angles remain close to 90°, which is the ideal situation where the separation angle is maximum. Therefore, it is established that the transformation matrix obtained by optimization provides a good tradeoff between all the angles.

The previous examples have demonstrated the capability of the proposed transformation matrix calculation using constraint optimization to overcome the special case for sensor-actuator FDI defined in section 3.4 and the undesirable FDI features

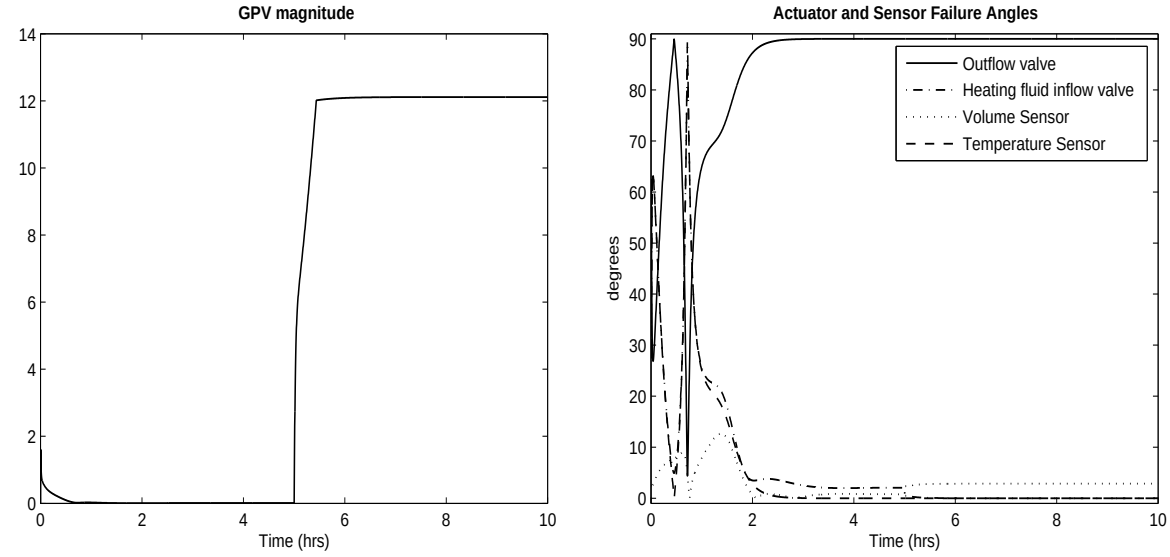

(a) (b)

Figure 7.5: Untransformed GPV

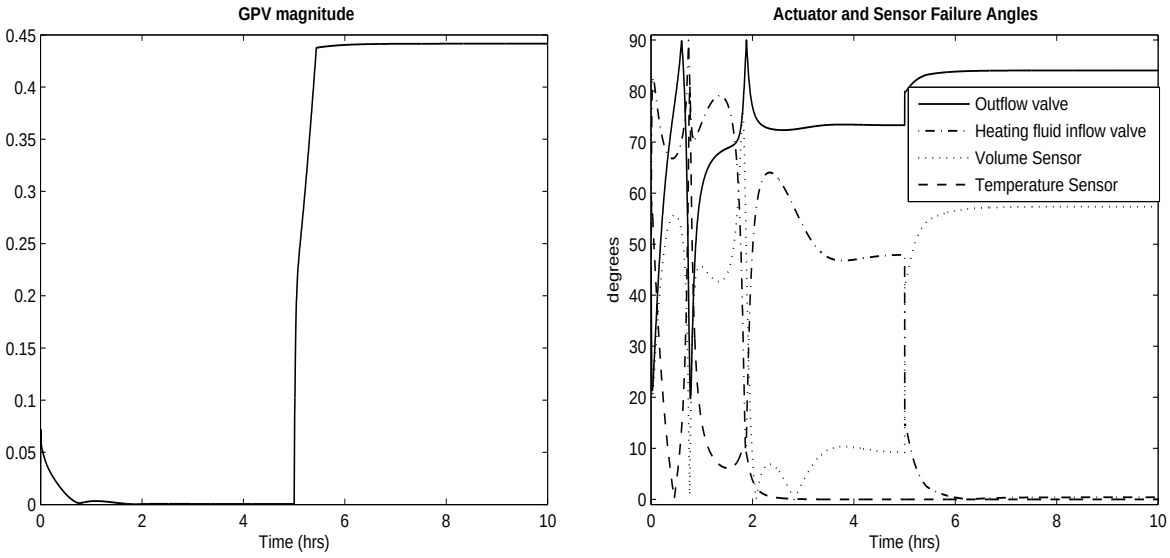

(a) (b)

Figure 7.6: Transformed GPV

$\measuredangle\,(^\circ)$	B_n^{ov}	B_n^{hv}
B_n^{ov}	-	89.99
B_n^{hv}	89.99	-
SP^v	0	62.58
SP^t	89.99	0

Table 7.1: Transformed reference directions angles

due to the nonlinear dynamics of the system.

7.3 Disturbance decoupling results

To illustrate the effect of implementing disturbance decoupling in the FDI algorithm, a -50% temperature sensor fault is applied at *t=2.5 hours*, followed by a 50% low inlet flow disturbance, F_{in}, at *t= 6 hours*, for ΔV=40% and ΔT=10%. The corresponding time histories are shown in Figs. 7.7, 7.8 and 7.9.

In figure 7.10 (FDI without disturbance decoupling) it is observed that the $|GPV|$ is significantly decreased after the disturbance is applied. Since for small fault sizes the magnitude increment after a fault is not very large, this reduction may be enough to cause a misdetection. However, when disturbance decoupling is incorporated into the FDI algorithm, this situation is overcome as illustrated in figure 7.11, where the disturbance is rejected quickly, driving the $|GPV|_{faulty}$ back to its undisturbed value.

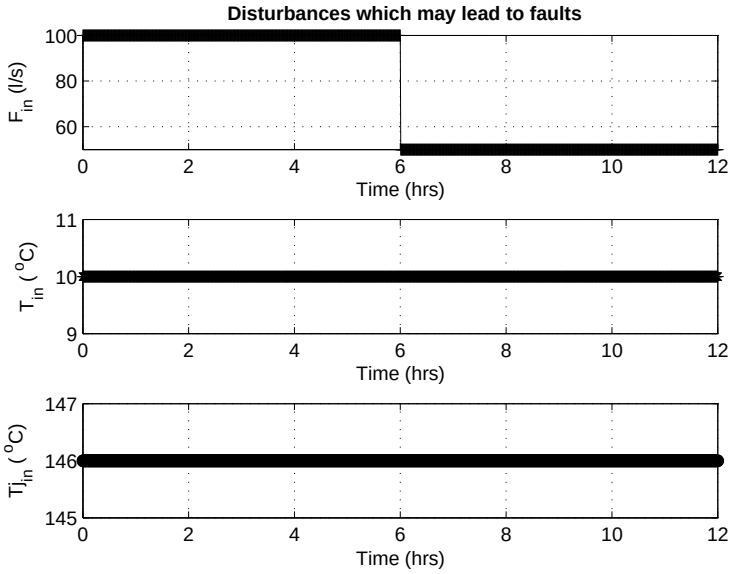

Figure 7.7: Disturbance time-histories

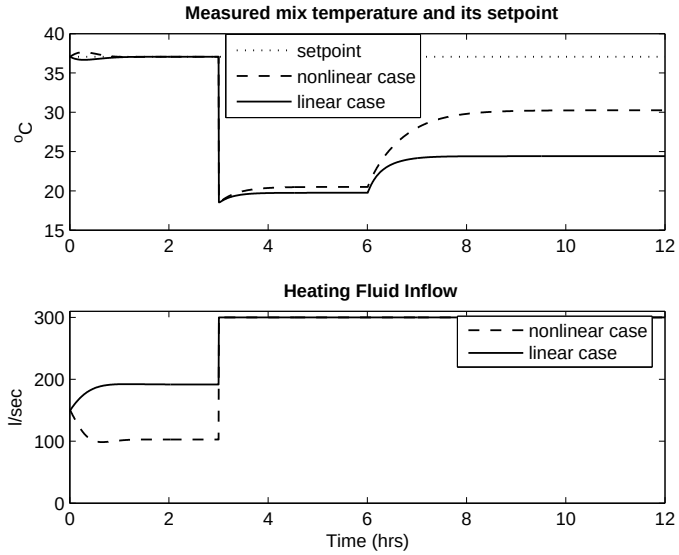

Figure 7.8: Time-histories for a -50% temperature sensor fault + 50% low inlet flow disturbance

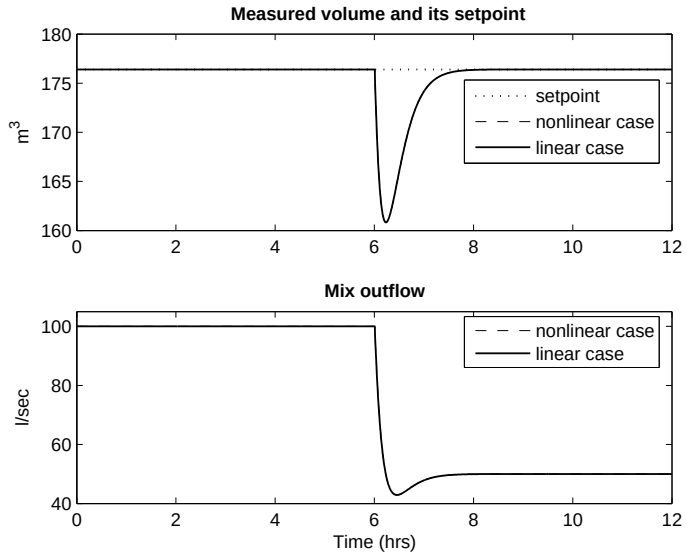

Figure 7.9: Time-histories for a -50% temperature sensor fault +50% low inlet flow disturbance

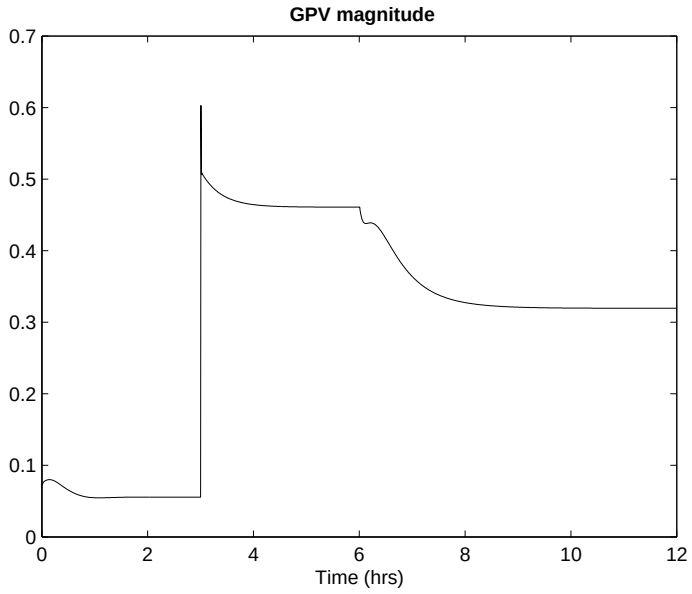

Figure 7.10: $|GPV|$ without disturbance decoupling

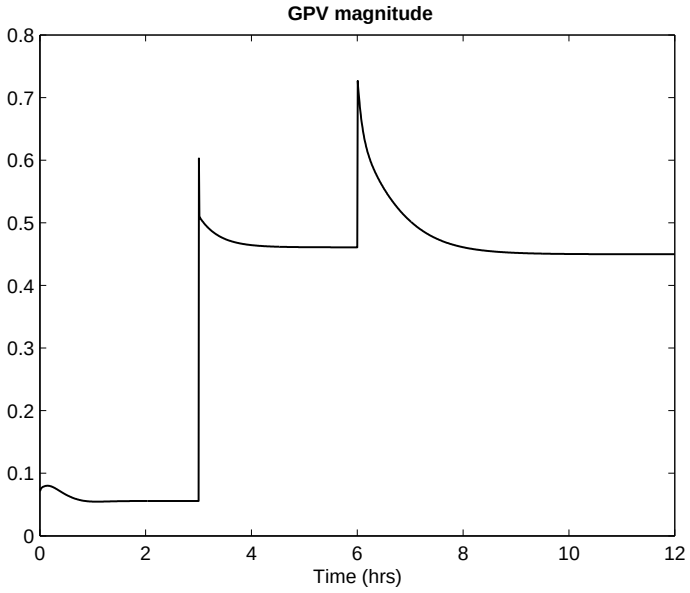

Figure 7.11: $|GPV|$ with disturbance decoupling

The effect of disturbances is even more significant in the $\angle GPV$ behavior as illustrated in figure 7.12. After the disturbance is applied, the temperature sensor $\angle GPV$ increases substantially, becoming larger than the volume sensor and outflow valve $\angle GPV$. As a result, the FDI algorithm detects a volume sensor fault instead, yielding an incorrect isolation. To avoid these false alarms, disturbance decoupling is implemented in the FDI algorithm to maintain the GPV directionality in the presence of disturbances, as portrayed in Fig. 7.13. It is observed that after the disturbance is applied at *t= 6 hours*, the temperature $\angle GPV$ is only slightly affected for a short period of time while the disturbance is completely rejected. Similarly, the other $\angle GPV$ are just trivially perturbed and keep their undisturbed directionality, allowing a clear isolation of the temperature sensor fault. Therefore, by incorporating disturbance

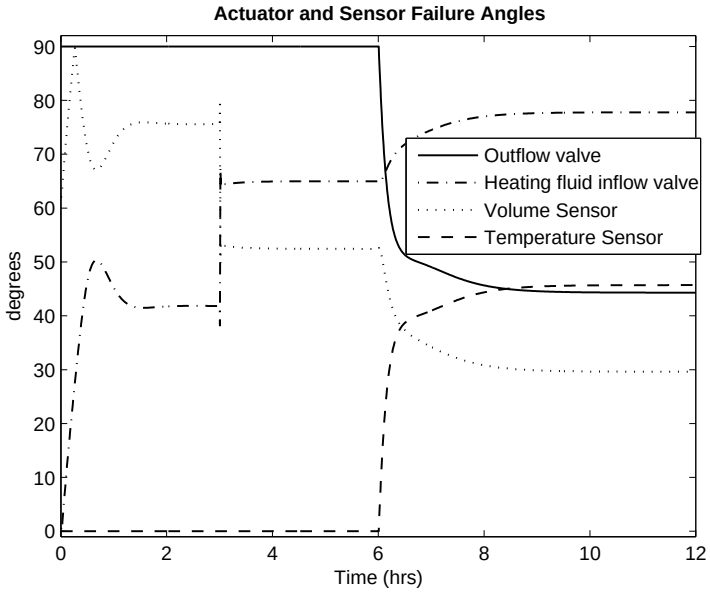

Figure 7.12: $\angle GPV$ without disturbance decoupling

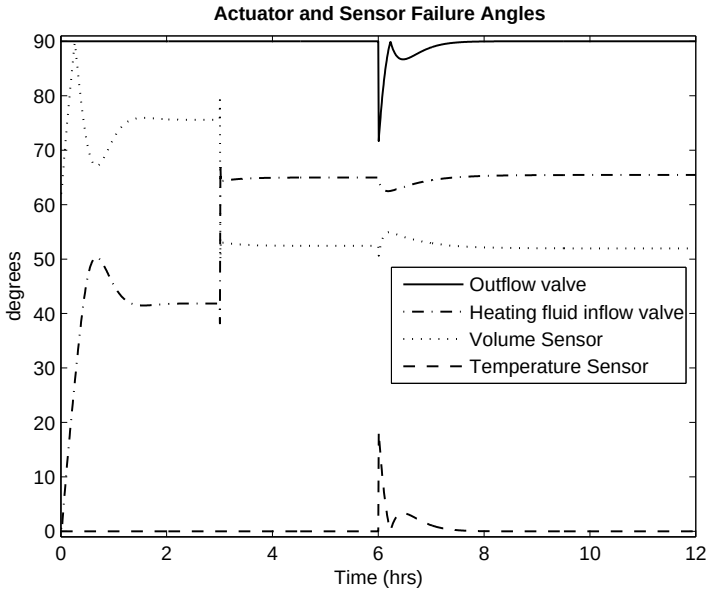

Figure 7.13: $\angle GPV$ with disturbance decoupling

decoupling, the FDI algorithm becomes robust to disturbance effects.

7.4 Decision maker results

The performance of the decision maker block using the four techniques presented in section 5.2 was evaluated applying 361 setpoint variations within the controller envelope. At each operating point, false alarms and misdetections were evaluated and counted for each threshold method, applying each fault with a magnitude of -50%. These results are displayed in a separate bar graph for each fault in appendix D. The average threshold logic performance for all the faults is illustrated in figure 7.14.

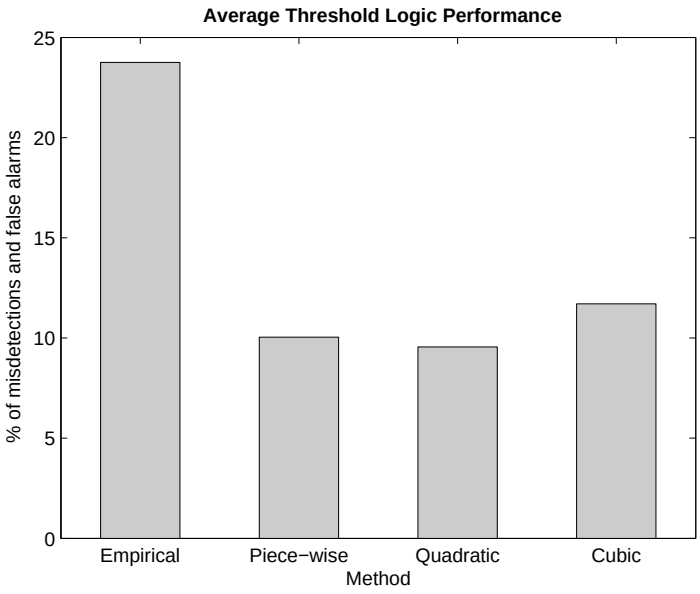

Figure 7.14: Average threshold logic performance

Figure 7.14 shows a poor overall performance for the empirical threshold with respect to false alarms and misdetections, since they were generated 23.75% of the time (87 times out of 361 cases). In contrast, the piece-wise linear, quadratic and cubic threshold logics provide substantially better performance in the controller envelope. They produce false alarms or misdetection rates only for 10.04% 9.56% and 11.7% of the setpoint variations applied, respectively. These percentages are satisfactory, since the performance test was done for a extended region around the nominal operating point with maximum variations of -35%$<\Delta V<$55% and -15%$<\Delta T<$20%.

Although the three analytic methods had similar performance in terms of false alarms and misdetection rates, the cubic and quadratic threshold logics provided faster detection rates for some fault scenarios. This is illustrated in figures 7.15, 7.16, 7.17 and 7.18, for a -30% heating fluid inflow valve fault applied at *t=1.5 hours* with ΔV=9% and ΔT=5%. The figures for other sensor and actuator time-histories are attached in appendix E. Figures 7.15-7.18 show the GPV fault display, a simple operator display of the FDI output. In this case all the threshold methods isolate the fault, but the detection time is significantly different. The empirical threshold logic takes 34 minutes to detect the fault, which is ineffective in real processes. The piece-wise linear threshold detects the fault after 24 minutes, which is still too long to be viable in actual plants. The quadratic and cubic approaches are able to detect the fault after 14 minutes, which is significantly better than the other two methods. This detection time is probably acceptable, since the JCSTR has large time constants. Even though the quadratic and cubic logics provide the same detection time, the latter yields a false temperature fault alarm during the first two minutes of the detection.

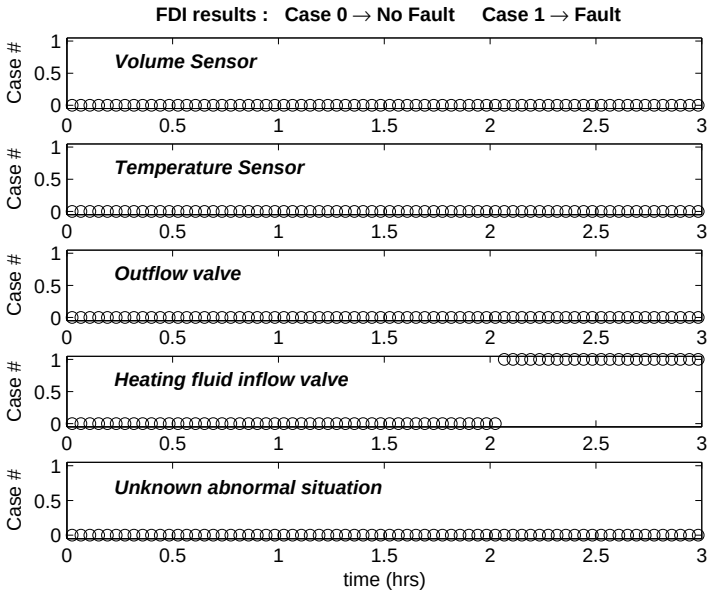

Figure 7.15: FDI results using empirical threshold scheduled logic

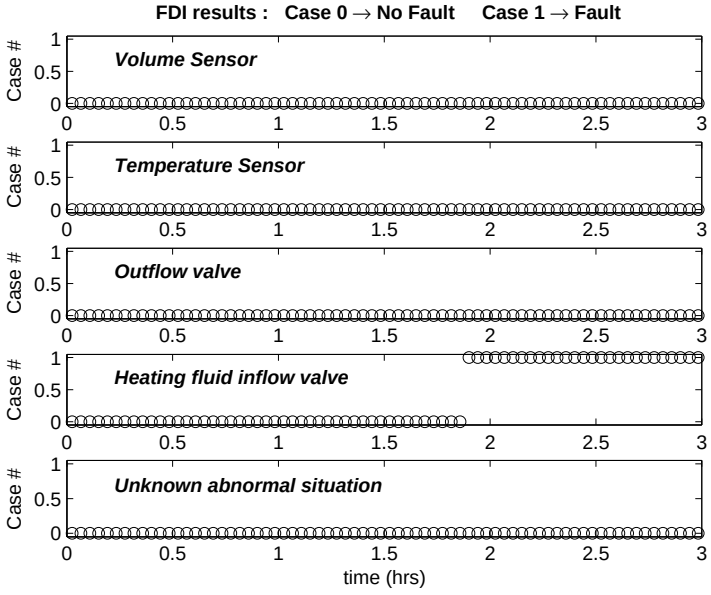

Figure 7.16: FDI results using piece-wise linear threshold logic

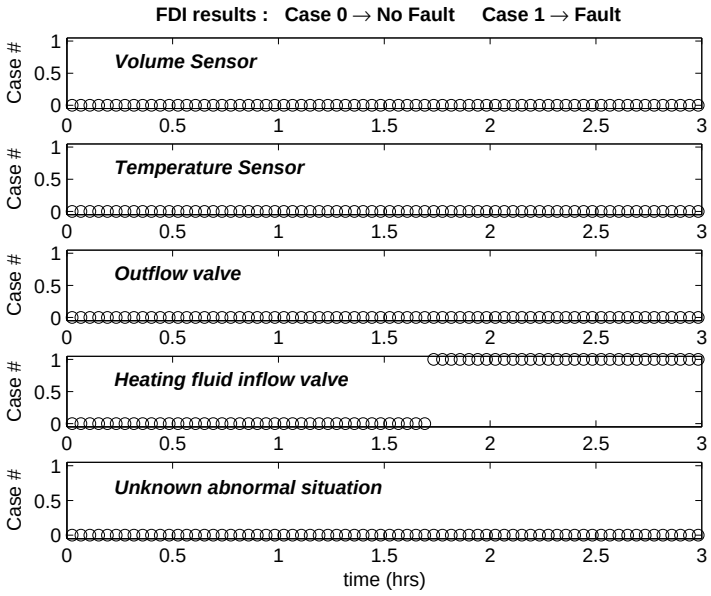

Figure 7.17: FDI results using quadratic threshold logic

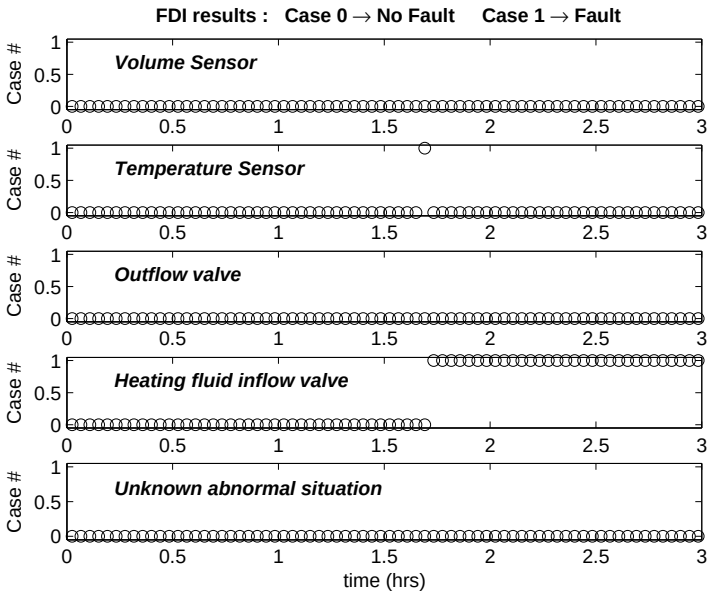

Figure 7.18: FDI results using cubic threshold logic

Evaluating the strengthens and weakness of each detection method, the quadratic threshold logic presents the best tradeoff between detection speed and false alarms and misdetection rates.

Chapter 8

Thesis Observations

8.1 Summary and conclusions

1. An extension of the generalized parity vector technique has been developed, implemented and tested using a JCSTR model.

2. A new systematic approach to calculate an optimal transformation matrix has been effectively developed, enhancing the FDI performance and its scope in terms of the number of faults that can be isolated and disturbances that can be decoupled.

3. The special case when an actuator fault GPV direction lies on a sensor fault plane has been clarified and isolation improved by extending the transformation approach. Additional logic has been added to deal with this case for improved actuator fault isolation.

4. A new approach for disturbance decoupling has been incorporated in the stable factorization framework to improve the FDI robustness.

5. Four novel threshold logics have been proposed to implement a robust decision maker block. Each technique has been evaluated considering detection speed, false alarms and misdetection rates, to select the one that provides the best tradeoff.

6. Robustness analysis has been successfully performed throughout the controller envelope, showing the FDI capability to handle the operating point and fault size variability.

7. Extensive simulation analysis have been successfully performed showing the validity of the different aspects analyzed in this research.

8.2 Future work

1. Even though the robustness has been significantly improved by incorporating an optimal transformation matrix calculation, disturbance decoupling and adaptive threshold logics, there is still some sensitivity of the GPV technique with respect to modelling errors. For future work, it is proposed to make the GPV technique adaptive depending on the operating point by incorporating a model identification module to handle variable dynamics. This improvement may also necessitate the online calculation of the transformation matrix using optimization to guarantee the best separation for the set of GPV angles at each operating point; this too can be investigated.

2. So far a constant transformation matrix has been used. However, future work

may be oriented to the calculation of a transfer function transformation matrix $T_r(s)$ to make the sensor fault directional and thus improve the FDI performance.

3. Although the results obtained using a simple 3D piece-wise linear threshold were satisfactory, future research can improve the false alarm and misdetection rates further, by obtaining it using a more sophisticated technique such as spline or 3D-interpolation.

4. Since in this research concurrent faults were not considered, the isolation block was implemented using a fixed angle threshold. However, further research should study the implementation of an adaptive isolation block which may be able to extend this technique to detect simultaneous faults regardless the nonlinearities involves.

5. Our future research will implement this FDI technique using the actual model and data originating from one of the pilot plant facilities involved in the Petroleum Applications of Wireless Systems (PAWS) project. This will allow the GPV technique performance to be tested for large scale processes.

Bibliography

[1] P. J. Antsaklis. Proper stable transfer matrix factorization and internal system descriptions. *IEEE Transactions on automatic control*, 31(7):634–638, 1986.

[2] E. Y. Chow and A. S. Willsky. Analytical redundancy and the design of robust failure detection systems. *IEEE Transactions on automatic control*, 29(7):603–614, 1984.

[3] P. M. Frank. Residual evaluation for fault diagnosis based on adaptive fuzzy thresholds. *IEE Colloquium on Qualitative and Quantitative Modelling Methods for Fault Diagnosis*, April 1995.

[4] J. J. Gertler. Survey of model-based failure detection and isolation in complex plants. *IEEE Control systems magazine*, 8(6):3–11, 1988.

[5] J. J. Gertler. Fault detection and isolation using parity relations. *Control Eng. Practice*, 5(5):653–661, 1997.

[6] J. J. Gertler. *Fault Detection and Diagnosis in Engineering Systems*. Marcel Dekker, Inc., 1998.

[7] J. J. Gertler and R. Monajemy. Generating directional residuals with dynamic parity relations. *Automatica*, 31(4):627–635, 1995.

[8] J. J. Gertler and D. Singer. A new structural framework for parity equation-based failure detection and isolation. *Automatica*, 26(2):381–388, 1990.

[9] F. Gustafsson. Stochastic fault diagnosability in parity spaces. *Proc. IFAC World Congress*, 2002.

[10] F. Hamelin, D. Sauter, and M. Aubrun. Fault diagnosis in systems using directional residuals. *Proc. 33rd IEEE Conference on Decision and Control*, 1994.

[11] D. C. Lay. *Linear Algebra and its Applications.* Addison-Wesley, 2^{nd} edition, 1997.

[12] C. C. MacDuffee. *Vectors and Matrices.* Math. Assoc. Amer., 1943.

[13] M. Omana and J. H. Taylor. Robust fault detection and isolation using a parity equation implementation of directional residuals. *Proc. IEEE Advanced Process Control Applications for Industry Workshop (APC2005)*, 2005.

[14] A.D. Pouliezos and G. S. Stavrakakis. *Real Time Fault Monitoring of Industrial Processes.* Kluwer Academic Publishers., 1994.

[15] A. Sayda. A benchmark model of a jacketed stirred tank heater for fault detection and isolation. May 2004.

[16] S. Simani, C. Fantuzzi, and R. J. Patton. *Model-based Fault diagnosis in Dynamic Systems Using Identification Techniques.* Springer, 2003.

[17] V. Venkatasubramanian, R. Rengaswamy, and S. N. Kavuri. A review of process fault detection and diagnosis, part ii: Qualitative models and search strategies. *Computers and chemical engineering*, 27:313–326, 2003. Elsevier Science Ltd.

[18] V. Venkatasubramanian, R. Rengaswamy, K. Yin, and S. N. Kavuri. A review of process fault detection and diagnosis, part i: Quantitative model-based methods. *Computers and chemical engineering*, 27:293–311, 2003. Elsevier Science Ltd.

[19] V. Venkatasubramanian, R. Rengaswamy, K. Yin, and S. N. Kavuri. A review of process fault detection and diagnosis, part iii: Process history based methods. *Computers and chemical engineering*, 27:327–346, 2003. Elsevier Science Ltd.

[20] M. Vidyasagar. *Control System synthesis: A Factorization Approach*. The MIT Press, 1985.

[21] N. Viswanadham, J. H. Taylor, and E.C. Luce. A Frequency Domain Approach to Failure Detection and Isolation with Application to GE-21 Turbine Engine Control Systems. *Control-Theory and advanced technology*, 3(1):45–72, MITA press, 1987.

[22] A. S. Willsky. A survey of design methods for failure detection in dynamic systems. *Automatica*, 12(6):601– 611, 1984.

Appendix A

JCSTR Dynamic Model

In this JCSTR, see figure A.1, the tank inlet stream is received from another process unit and there is a heat transfer fluid circulating through the jacket to heat the fluid in the tank. The objective is to control the temperature and the volume inside the tank by varying the jacket inlet valve flow rate (the temperature control or TC loop) and tank outlet valve flow rate (the level control or LC loop) respectively.

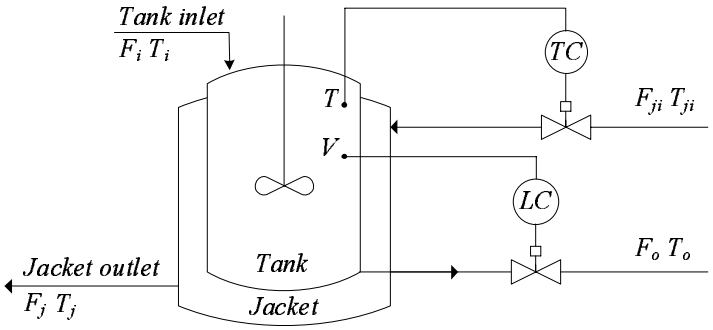

Figure A.1: Jacketed continuously stirred tank reactor

In order to derive the dynamic modeling equations of the tank and jacket temperatures, the following assumptions were made:

- Liquids have constant density and heat capacity.

- Mixing in both the tank and jacket are perfect.
- The tank inlet flow rate, jacket flow rate, tank inlet temperature and jacket inlet temperature may change (these are the inputs).
- The rate of heat transfer from the jacket to the tank is governed by the equation $Q = U\,A(T_j - T)$, where U is the overall heat transfer coefficient and A is the area for heat transfer and is given by equation $A = \frac{\pi D_r^2}{4} + \frac{4V}{D_r}$.

The following equations describe the ODE model for the JCSTR reactor [15] and the notation used is listed below.

$$\dot{V} = F_{in} - F_{out} \tag{A.1}$$

$$\dot{T} = \frac{F_{in}\,(T_{in} - T)}{V} + \frac{U\,A\,(T_j - T)}{V\,\rho\,C_p} \tag{A.2}$$

$$\dot{T_j} = \frac{F_{Jin}\,(T_{Jin} - T_j)}{V_j} + \frac{U\,A\,(T_j - T)}{V_j\,\rho\,C_p} \tag{A.3}$$

NOTATION

Subscripts

i	Inlet
j	Jacket
J_{in}	Jacket inlet

Variables

A	Area for heat transfer
D_r	Diameter of the reactor
C_p	Heat capacity (energy/mass*temp)
F	Volumetric flowrate (volume/time)
ρ	Density (mass/vol)
T	Temperature
Q	Rate of heat transfer (energy/time)
U	Heat transfer coefficient (energy/time*area*temp)
V	Volume

Parameter values

D_r	5 m
C_p	4.1868*1000 *(J/kg.K)*
F_{in}	0.1 (m^3/s)
ρ	997.95 (kg/m^3)
T_{in}	283 ^oK
F_{Jout}	0.15 (m^3/s)
V_j	9 m^3
T_{Jin}	419 ^oK
U	851.74 $(W/m^2.K)$

Operating point 1

V_o	180 m^3
T_o	306.5824 ^oK
T_j	377.2784 ^oK

Operating point 2

V_o 126 m^3

T_o 306.6937 ^oK

T_j 403.2040 ^oK

Appendix B

Statistical Parameters

B.1 Quadratic fitting

This section presents the parameters corresponding to the surface-fit performed in section 5.2.3 using a free trial demo of TableCurv 3D V4.0 ©SYSTAT Software Inc. The obtained fitting has the quadratic form $z = a+bx+cy+dx^2+ey^2+fxy$, that was rewritten in terms of the variables to provide the following equation for the $|GPV|_{ff}$:

$$|GPV|_{ff} = a + b\Delta V + c\Delta T + d\Delta V^2 + e\Delta T^2 + f\Delta V\Delta T \tag{B.1}$$

The polynomial coefficients and the different statistical parameters describing equation B.1 are attached below.

Rank 25 Eqn 310 $z=a+bx+cy+dx^2+ey^2+fxy+gx^3+hy^3+ixy^2+jx^2y$

r^2 Coef Det	DF Adj r^2	Fit Std Err	F-value
0.8542737926	0.8532417373	0.0185004739	920.36283512

Parm	Value	Std Error	t-value	95.00% Confidence Limits		P>|t|
a	0.03616	0.00110	32.7521	0.03399	0.03832	0.00
b	-0.3263	0.01292	-25.247	-0.3516	-0.3009	0.00
c	0.45740	0.03228	14.1673	0.39406	0.52073	0.00
d	2.74342	0.07843	34.9768	2.58956	2.89728	0.00
e	10.9901	0.43410	25.3170	10.1385	11.8417	0.00
f	-9.7232	0.34089	-28.522	-10.391	-9.0544	0.00
g	-3.1157	0.12826	-24.291	-3.3673	-2.8641	0.00
h	-47.390	3.37834	-14.027	-54.017	-40.762	0.00
i	26.4192	2.57689	10.2523	21.3642	31.4741	0.00
j	5.47947	0.87050	6.29462	3.77186	7.18709	0.00

X at Fn Zmin	Y at Fn Zmin	Fn Zmin
0.1199909132	0.0255321139	0.0234681045

X at Fn Zmax	Y at Fn Zmax	Fn Zmax
0.55	-0.16	1.5328709632

Procedure
GaussElim

r^2 Coef Det	DF Adj r^2	Fit Std Err
0.8542737926	0.8532417373	0.0185004739

Source	Sum of Squares	DF	Mean Square	F Statistic	P>F
Regr	2.8350929	9	0.31501032	920.363	0.00000
Error	0.48362403	1413	0.000342267		
Total	3.3187169	1422			

Description: gpvff.prn, X , Y , Z

X Variable:

Xmin:	-0.35	Xmax:	0.55	Xrange:	0.9
Xmean:	0.188186929	Xstd:	0.2321354458		

Y Variable:

Ymin:	-0.16	Ymax:	0.2	Yrange:	0.36
Ymean:	0.0186437105	Ystd:	0.0816448449		

Z Variable:

Zmin:	1.261e-05	Zmax:	0.24575	Zrange:	0.24573739
Zmean:	0.0809758678	Zstd:	0.0483098073		

B.2 Cubic fitting

This section presents the parameters corresponding to the surface-fit performed in section 5.2.4. The resulting fitting was a bivariate cubic polynomial of the form $z = a+bx+cy+dx^2+ey^2+fxy+gx^3+hy^3+ixy^2+jx^2y$. By rewriting this equation in terms of the variables, the $|GPV|_{ff}$ is defined as:

$$\begin{aligned} |GPV|_{ff} &= a + b\Delta V + c\Delta T + d\Delta V^2 + e\Delta T^2 + f\Delta V\Delta T + \\ &\quad g\Delta V^3 + h\Delta T^3 + i\Delta V\Delta T^2 + j\Delta V^2\Delta T \end{aligned} \tag{B.2}$$

The polynomial coefficients and the different statistical parameters describing equation B.2 are attached below.

Rank 25 Eqn 310 $z=a+bx+cy+dx^2+ey^2+fxy+gx^3+hy^3+ixy^2+jx^2y$

r^2 Coef Det	DF Adj r^2	Fit Std Err	F-value
0.8542737926	0.8532417373	0.0185004739	920.36283512

Parm	Value	Std Error	t-value	95.00% Confidence Limits		P>|t|
a	0.03616	0.00110	32.7521	0.03399	0.03832	0.00
b	-0.3263	0.01292	-25.247	-0.3516	-0.3009	0.00
c	0.45740	0.03228	14.1673	0.39406	0.52073	0.00
d	2.74342	0.07843	34.9768	2.58956	2.89728	0.00
e	10.9901	0.43410	25.3170	10.1385	11.8417	0.00
f	-9.7232	0.34089	-28.522	-10.391	-9.0544	0.00
g	-3.1157	0.12826	-24.291	-3.3673	-2.8641	0.00
h	-47.390	3.37834	-14.027	-54.017	-40.762	0.00
i	26.4192	2.57689	10.2523	21.3642	31.4741	0.00
j	5.47947	0.87050	6.29462	3.77186	7.18709	0.00

X at Fn Zmin	Y at Fn Zmin	Fn Zmin
0.1199909132	0.0255321139	0.0234681045

X at Fn Zmax	Y at Fn Zmax	Fn Zmax
0.55	-0.16	1.5328709632

Procedure
GaussElim

r^2 Coef Det	DF Adj r^2	Fit Std Err
0.8542737926	0.8532417373	0.0185004739

Source	Sum of Squares	DF	Mean Square	F Statistic	P>F
Regr	2.8350929	9	0.31501032	920.363	0.00000
Error	0.48362403	1413	0.000342267		
Total	3.3187169	1422			

Description: gpvff.prn, X , Y , Z

X Variable:

Xmin:	-0.35	Xmax:	0.55	Xrange:	0.9
Xmean:	0.188186929	Xstd:	0.2321354458		

Y Variable:

Ymin:	-0.16	Ymax:	0.2	Yrange:	0.36
Ymean:	0.0186437105	Ystd:	0.0816448449		

Z Variable:

Zmin:	1.261e-05	Zmax:	0.24575	Zrange:	0.24573739
Zmean:	0.0809758678	Zstd:	0.0483098073		

Appendix C

Complementary Figures for Section 7.2

Figures C.1 and C.2 illustrate the time histories for a -50% bias outflow valve fault applied at t=5 hours for a temperature setpoint variation of +5% and a volume setpoint variation of +5%.

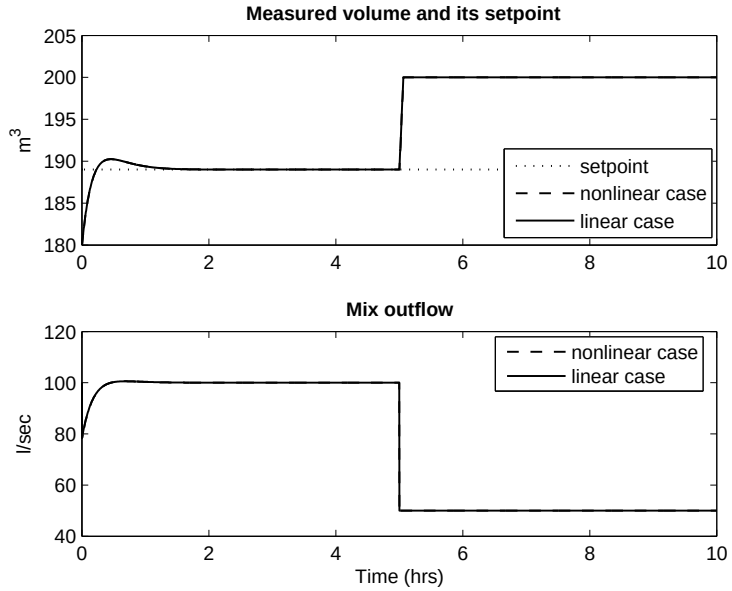

Figure C.1: Time histories for a -50% bias outflow valve fault

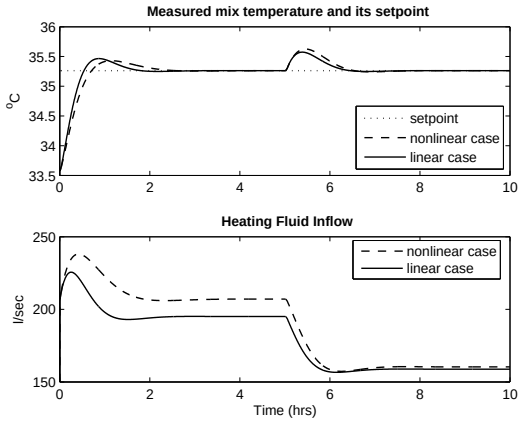

Figure C.2: Time histories for a -50% bias outflow valve fault

Figures C.3, C.4, C.5 and C.6 correspond to the time histories for a -50% volume sensor fault at *t=5 hours* with ΔV=7% and ΔT=5%. Figures C.7 and C.8, show the $|GPV|$ with and without using constraint 3 for this fault scenario.

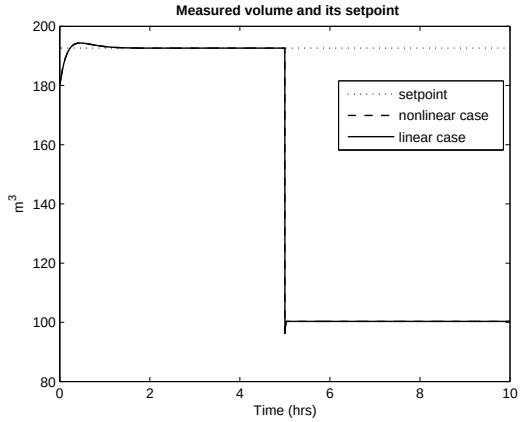

Figure C.3: Time-histories for a -50% volume sensor fault

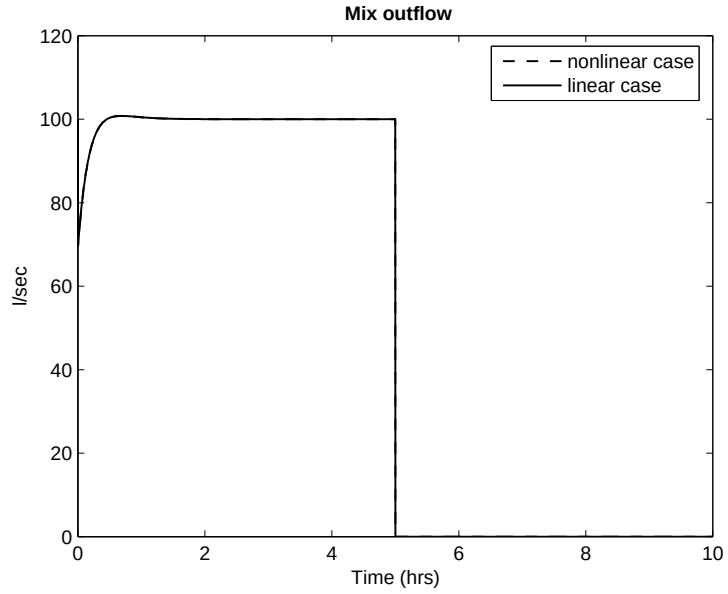

Figure C.4: Time-histories for a -50% volume sensor fault

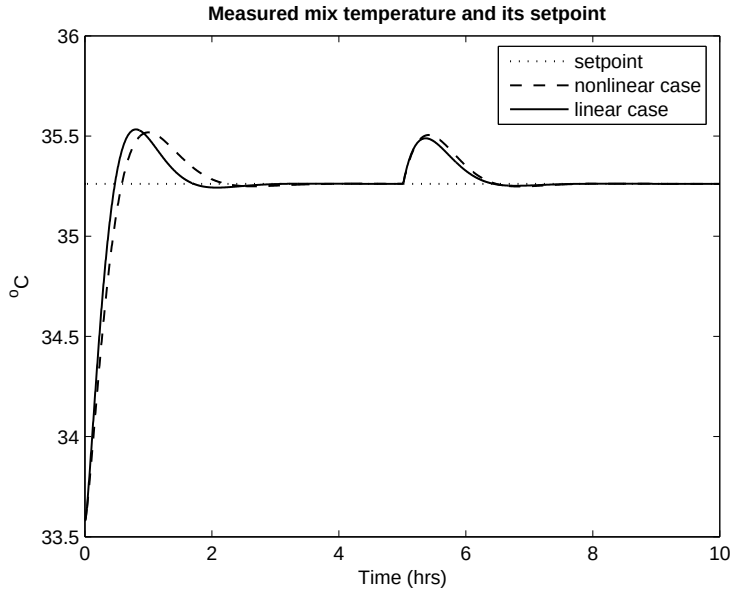

Figure C.5: Time-histories for a -50% volume sensor fault

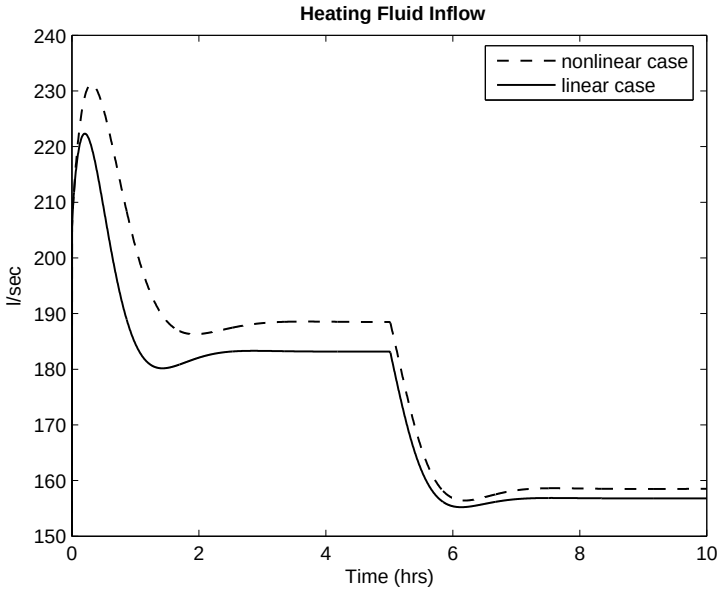

Figure C.6: Time-histories for a -50% volume sensor fault

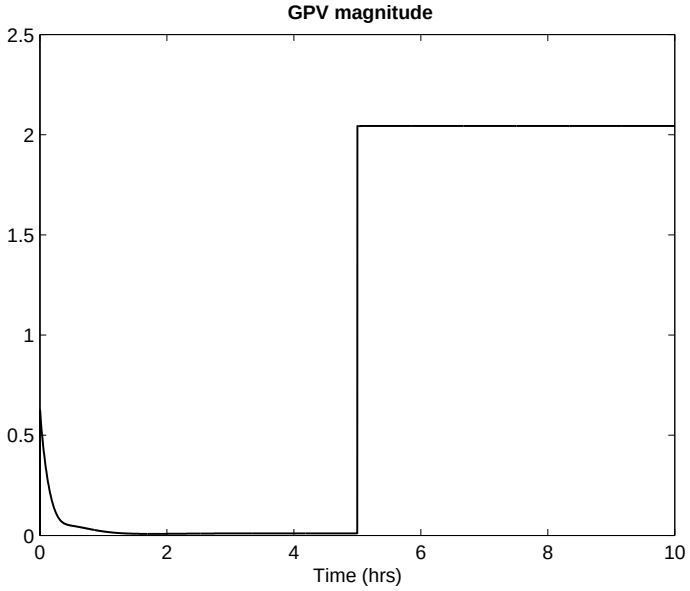

Figure C.7: $|GPV|$ without using constraint 3

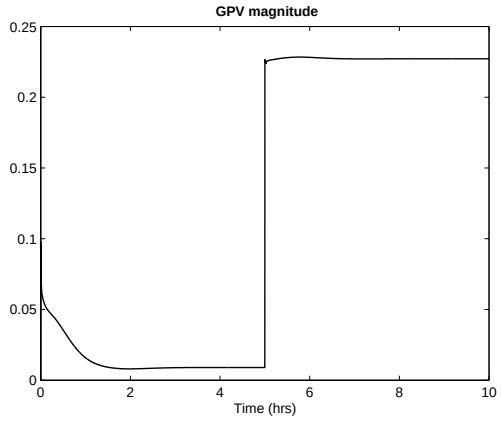

Figure C.8: $|GPV|$ using constraint 3

Figures C.9, C.10, C.11 and C.12 show the time histories for a -50% heating fluid inflow valve fault at *t=5 hours* with ΔV=7% and ΔT=3%.

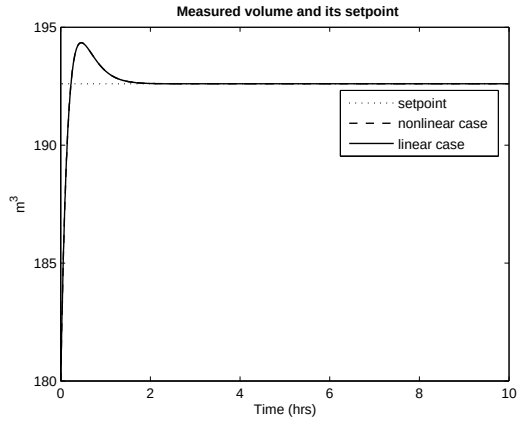

Figure C.9: Time-histories for a -50% heating fluid inflow valve fault

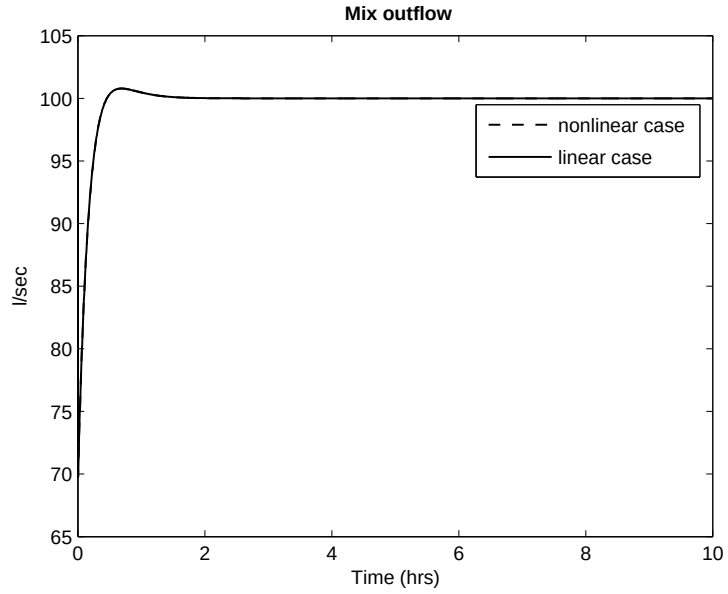

Figure C.10: Time-histories for a -50% heating fluid inflow valve fault

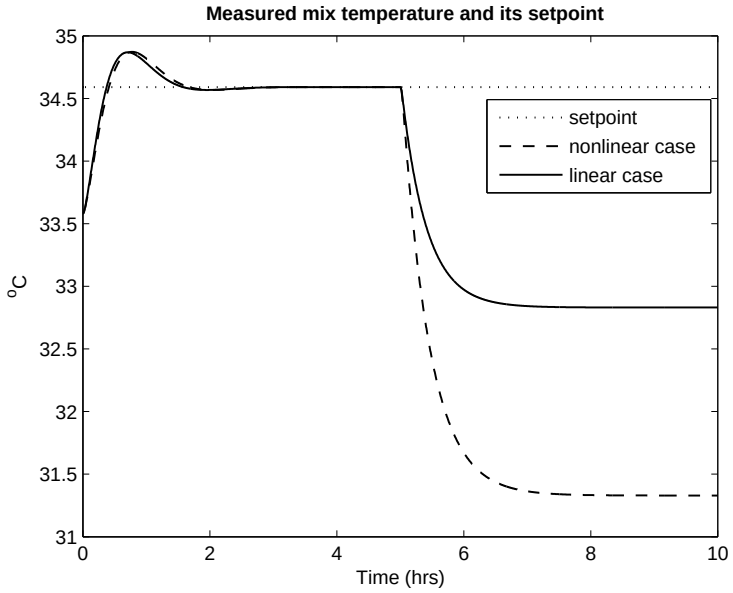

Figure C.11: Time-histories for a -50% heating fluid inflow valve fault

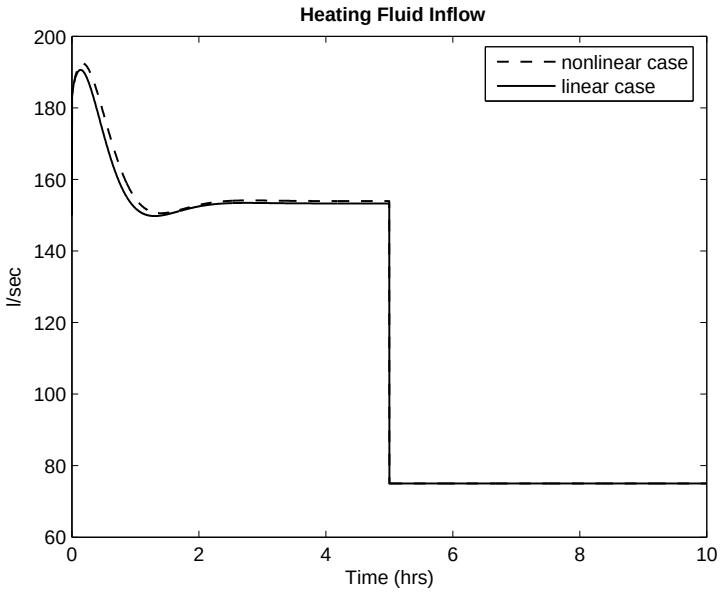

Figure C.12: Time-histories for a -50% heating fluid inflow valve fault

Appendix D

Complementary Bar Graphs for Section 7.4

The followings bar graphs show the performance comparison between the different threshold logics along the controller envelope for each fault.

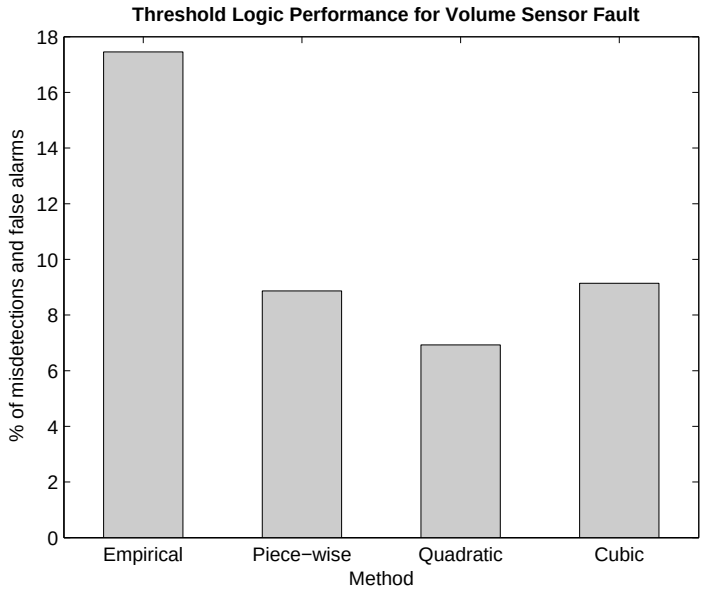

Figure D.1: Threshold logic performance for volume sensor fault

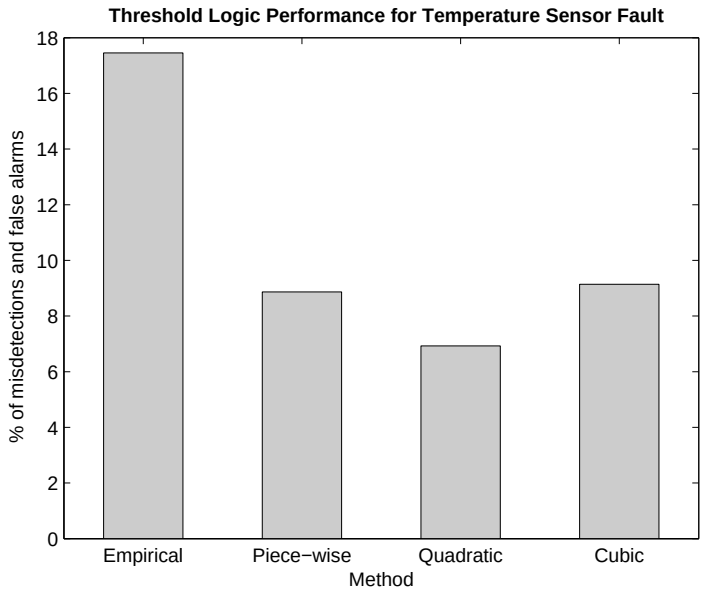

Figure D.2: Threshold logic performance for temperature sensor fault

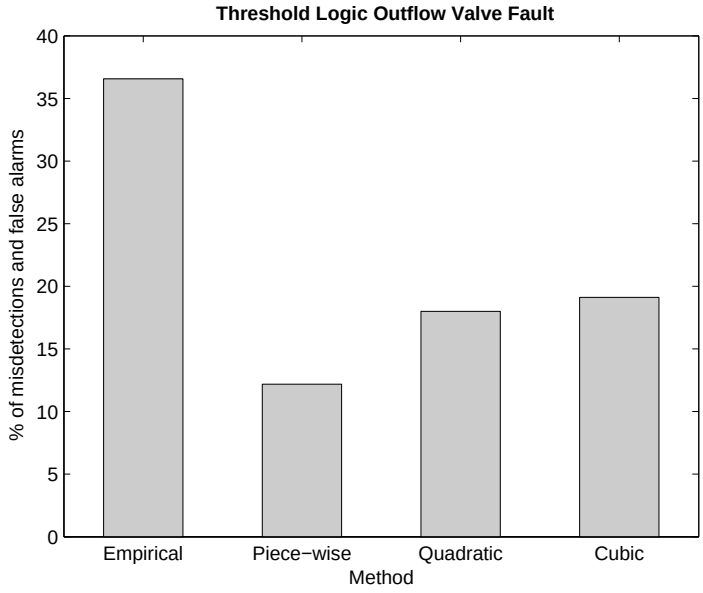

Figure D.3: Threshold logic performance for outflow valve fault

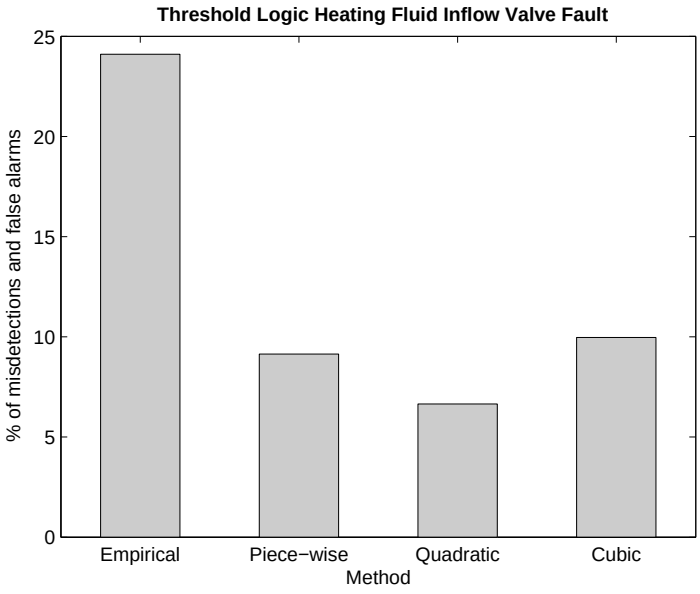

Figure D.4: Threshold logic performance for heating fluid inflow valve fault

Appendix E

Complementary Time-Histories Figures for Section 7.4

The following figures correspond to the time histories for a -30% heating fluid inflow valve fault applied at *t=1.5 hours* with ΔV=9% and ΔT=5%.

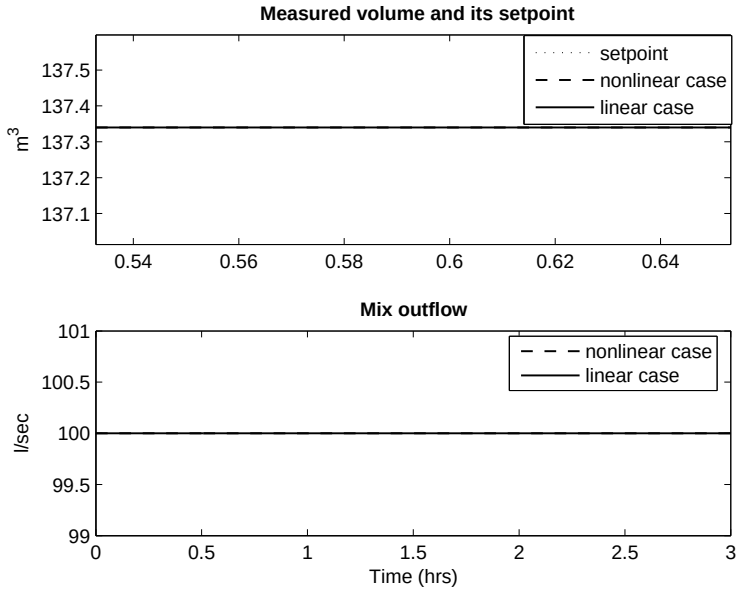

Figure E.1: Time histories for a -30% bias heating inflow valve fault

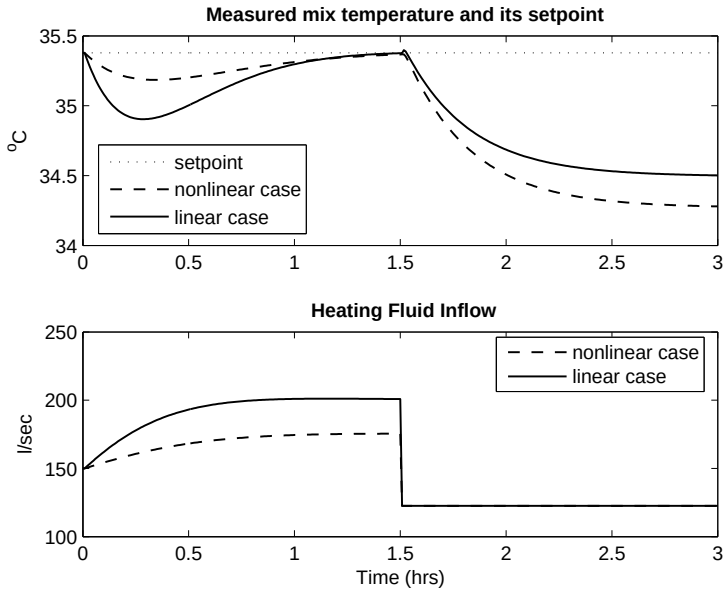

Figure E.2: Time histories for a -30% bias heating inflow valve fault

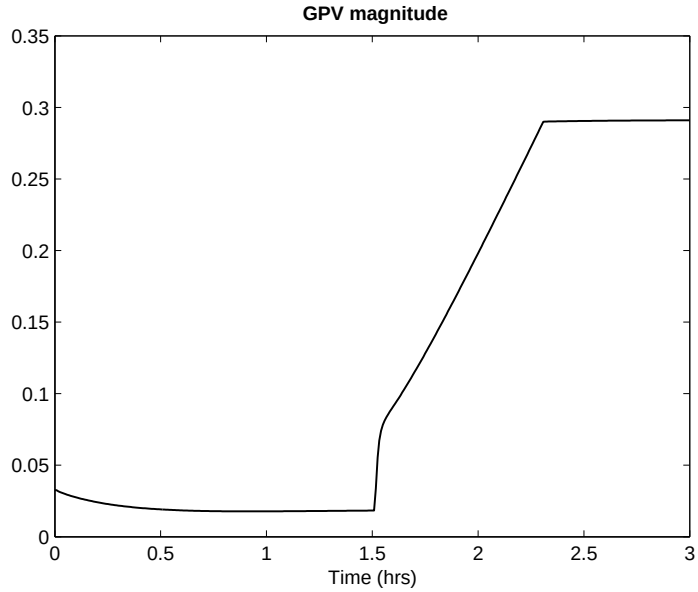

Figure E.3: Time histories for a -30% bias heating inflow valve fault

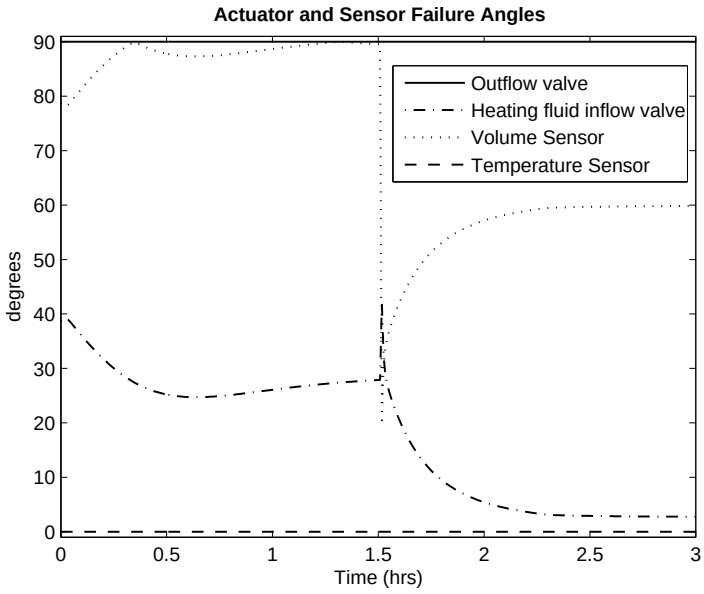

Figure E.4: Time histories for a -30% bias heating inflow valve fault

Appendix F

Optimization Routine Results

The transformation matrix optimization method presented in chapter 4 was tested using different random initial values for T_o. The optimization results for ten different T_{oi} are presented below, with its corresponding T_{ri} and set of angles. These angles are obtained by transforming the original set of reference directions with the corresponding T_{ri}.

From the results it is demonstrated that even though the solution for T_r is not unique, it is always optimal and provides a set of angles with maximum separation. By comparing the values in tables F.1, F.2, F.3, F.4, F.5, F.6, F.7, F.8, F.9 and F.10, it is observed that the difference between each set of transformed reference directions angles is $\leq 10^{-4}$. Since the angle range is between 0° and 90°, a variation $\leq 10^{-4}$ is neglectable.

Therefore, it is stated that the transformation matrix optimization method guarantees the same optimal set of angles, regardless the initial values of T_o and the results obtained for T_r.

$$T_{01} = \begin{bmatrix} 0.44470336435319 & 0.92181297074480 & 0.40570621306210 \\ 0.61543234810009 & 0.73820724581067 & 0.93546969910761 \\ 0.79193703742704 & 0.17626614449462 & 0.91690443991341 \end{bmatrix} \tag{F.1}$$

$$T_{r1} = \begin{bmatrix} -0.05194676496515 & 0.94094391898361 & 0.00305224773755 \\ -0.09998790168314 & -0.5669016282185 & -0.0362556743034 \\ -0.14897393939406 & 0.05238696416200 & 0.02326963926715 \end{bmatrix} \tag{F.2}$$

$\measuredangle\,(^\circ)$	B_n^{ov}	B_n^{hv}
B_n^{ov}	0	89.99996752797870
B_n^{hv}	89.99996752797870	0
SP^v	0	62.58939356852625
SP^t	89.99996484981651	0

Table F.1: Transformed reference directions angles for T_{r1}

$$T_{02} = \begin{bmatrix} 0.41027020699095 & 0.35286813221700 & 0.13889088195695 \\ 0.89364953091353 & 0.81316649730376 & 0.20276521856027 \\ 0.05789130478427 & 0.00986130066092 & 0.19872174266149 \end{bmatrix} \tag{F.3}$$

$$T_{r2} = \begin{bmatrix} 0.11369096195394 & -0.6458719019600 & -0.0023668562260 \\ 0.03791607953446 & 0.60021879239988 & 0.03724041891269 \\ 0.11708564745205 & 0.43276987807864 & -0.0097618493320 \end{bmatrix} \tag{F.4}$$

$\measuredangle\,(^\circ)$	B_n^{ov}	B_n^{hv}
B_n^{ov}	0	89.99953964077456
B_n^{hv}	89.99953964077456	0
SP^v	0	62.58939117101704
SP^t	89.99953951118647	0

Table F.2: Transformed reference directions angles for T_{r2}

$$T_{03} = \begin{bmatrix} 0.50281288399625 & 0.30461736686939 & 0.68222322359138 \\ 0.70947139270339 & 0.18965374754717 & 0.30276440077661 \\ 0.42889236534100 & 0.19343115640522 & 0.54167385389809 \end{bmatrix} \tag{F.5}$$

$$T_{r3} = \begin{bmatrix} 0.00684355568779 & 0.51013273334789 & 0.03881700915275 \\ -0.12470406007108 & -0.5217548966185 & 0.00119043802266 \\ 0.10261674454854 & -0.6680804869893 & -0.0011420613477 \end{bmatrix} \tag{F.6}$$

$\measuredangle\,(^\circ)$	B_n^{ov}	B_n^{hv}
B_n^{ov}	0	89.99999353612962
B_n^{hv}	89.99999353612962	0
SP^v	0	62.58939332482288
SP^t	89.99993281175686	0

Table F.3: Transformed reference directions angles for T_{r3}

$$T_{04} = \begin{bmatrix} 0.15087297614976 & 0.86001160488682 & 0.49655244970310 \\ 0.69789848185986 & 0.85365513066277 & 0.89976917516961 \\ 0.37837300051267 & 0.59356291253968 & 0.82162916073534 \end{bmatrix} \tag{F.7}$$

$$T_{r4} = \begin{bmatrix} -0.0064844137364 & 0.98904292454219 & 0.03191726247386 \\ -0.1689847684377 & -0.1753628891650 & 0.00967501653221 \\ 0.07597583750139 & -0.3056289617605 & 0.02424317044179 \end{bmatrix} \tag{F.8}$$

$\measuredangle\,(^\circ)$	B_n^{ov}	B_n^{hv}
B_n^{ov}	0	89.99999989160767
B_n^{hv}	89.99999989160767	0
SP^v	0	62.58939325525691
SP^t	89.99995772311524	0

Table F.4: Transformed reference directions angles for T_{r4}

$$T_{05} = \begin{bmatrix} 0.64491038419384 & 0.34197061827022 & 0.53407901762660 \\ 0.81797434083925 & 0.28972589585624 & 0.72711321692968 \\ 0.66022755644160 & 0.34119356941488 & 0.30929015979096 \end{bmatrix} \tag{F.9}$$

$$T_{r5} = \begin{bmatrix} -0.08711218404002 & -0.7414312365354 & -0.0136640418577 \\ -0.05532928153552 & 0.21096751562309 & -0.0235362051771 \\ -0.10383014918281 & 0.50963434159004 & 0.02400609919095 \end{bmatrix} \tag{F.10}$$

$\measuredangle\,(^\circ)$	B_n^{ov}	B_n^{hv}
B_n^{ov}	0	89.99988127065217
B_n^{hv}	89.99988127065217	0
SP^v	0	62.58939326524080
SP^t	89.99982806050119	0

Table F.5: Transformed reference directions angles for T_{r5}

$$T_{06} = \begin{bmatrix} 0.83849604493808 & 0.70273991324038 & 0.69456724042555 \\ 0.56807246100778 & 0.54657115182911 & 0.62131013079541 \\ 0.37041355663212 & 0.44488020467291 & 0.79482108020093 \end{bmatrix} \tag{F.11}$$

$$T_{r6} = \begin{bmatrix} -0.03932720090354 & 0.38881383979846 & -0.0232257774446 \\ -0.10890457200911 & 0.71079334214074 & 0.02920610731514 \\ 0.14607122491273 & 0.63463971038040 & 0.01552341928696 \end{bmatrix} \tag{F.12}$$

$\measuredangle\,(^\circ)$	B_n^{ov}	B_n^{hv}
B_n^{ov}	0	89.99809045563512
B_n^{hv}	89.99809045563512	0
SP^v	0	62.58939160815882
SP^t	89.99808714477190	0

Table F.6: Transformed reference directions angles for T_{r6}

$$T_{07} = \begin{bmatrix} 0.95684344844488 & 0.17295614127524 & 0.25232934687399 \\ 0.52259034908071 & 0.97974689678884 & 0.87574189981807 \\ 0.88014220741133 & 0.27144725864180 & 0.73730598846526 \end{bmatrix} \tag{F.13}$$

$$T_{r7} = \begin{bmatrix} -0.00218712694053 & -1.0256743530600 & -0.0084723466339 \\ -0.16360978196500 & -0.1921181612975 & -0.0227990669791 \\ -0.10635512280000 & 0.31663055253980 & 0.03524684783400 \end{bmatrix} \tag{F.14}$$

$\measuredangle\,(^\circ)$	B_n^{ov}	B_n^{hv}
B_n^{ov}	0	89.99998385683553
B_n^{hv}	89.99998385683553	0
SP^v	0	62.58939337276787
SP^t	89.99986039038620	0

Table F.7: Transformed reference directions angles for T_{r7}

$$T_{08} = \begin{bmatrix} 0.98833493827763 & 0.51551175214076 & 0.22594986814445 \\ 0.58279168156123 & 0.33395147997176 & 0.57980687324960 \\ 0.42349625685105 & 0.43290659610673 & 0.76036500980434 \end{bmatrix} \tag{F.15}$$

$$T_{r8} = \begin{bmatrix} -0.1739158147028 & 0.13006657126393 & 0.01418622398380 \\ 0.04761845289118 & -0.3716369602068 & 0.02577756725531 \\ 0.03934227236902 & 1.02478805448115 & 0.03151098505494 \end{bmatrix} \tag{F.16}$$

$\measuredangle\,(^\circ)$	B_n^{ov}	B_n^{hv}
B_n^{ov}	0	89.99994906776206
B_n^{hv}	89.99994906776206	0
SP^v	0	62.58939335020708
SP^t	89.99992329329605	0

Table F.8: Transformed reference directions angles for T_{r8}

$$T_{09} = \begin{bmatrix} 0.13377274847343 & 0.62988784884231 & 0.45142482676248 \\ 0.20713272964136 & 0.37047682605190 & 0.04389532534714 \\ 0.60719894453953 & 0.57514777904747 & 0.02718512299667 \end{bmatrix} \tag{F.17}$$

$$T_{r9} = \begin{bmatrix} 0.07856732434048 & -0.8824952904922 & -0.0182393536750 \\ 0.12288454071054 & 0.48269828596790 & 0.02280464466386 \\ 0.04930268524697 & 0.20328009171653 & -0.0277736440901 \end{bmatrix} \tag{F.18}$$

$\measuredangle\,(^\circ)$	B_n^{ov}	B_n^{hv}
B_n^{ov}	0	89.99994610040091
B_n^{hv}	89.99994610040091	0
SP^v	0	62.58939337372820
SP^t	89.99870898922339	0

Table F.9: Transformed reference directions angles for T_{r9}

$$T_{010} = \begin{bmatrix} 0.01635493355000 & 0.05758108987829 & 0.71763442146570 \\ 0.19007458907973 & 0.36756803882634 & 0.69266939471779 \\ 0.58691847188467 & 0.63145116474444 & 0.08407906075044 \end{bmatrix} \tag{F.19}$$

$$T_{r10} = \begin{bmatrix} -0.1453086088619 & 0.67871863188700 & 0.02325273901571 \\ 0.11481299077676 & 0.86527568720472 & 0.01071147122075 \\ 0.06178354206512 & -0.0116743584305 & 0.03478273950457 \end{bmatrix} \tag{F.20}$$

$\measuredangle\,(^\circ)$	B_n^{ov}	B_n^{hv}
B_n^{ov}	0	89.99995744208242
B_n^{hv}	89.99995744208242	0
SP^v	0	62.58939331090693
SP^t	89.99995649941585	0

Table F.10: Transformed reference directions angles for T_{r10}

CURRICULUM VITAE

Candidate's full name:	Maira Omana
Universities attended:	Universidad Industrial de Santander, Bachelor in Electrical Engineering, 2001
Publications:	Robust Fault Detection and Isolation Using a Parity Equation Implementation of Directional Residuals, *Proc. APC 2005*
Conference Presentations:	IEEE Advanced Process Control Applications for Industry Workshop (APC2005), Vancouver, BC, may 9-11, 2005.